nature cell biology

Article

https://doi.org/10.1038/s41556-024-01552-2

Cohesin complex oligomerization maintains end-tethering at DNA double-strand breaks

Received: 27 November 2023

Accepted: 1 October 2024

Jamie Phipps[1,2], Mathias Toulouze[1,2], Cécile Ducrot[1,2], Rafaël Costa[1,2], Clémentine Brocas[1,2] & Karine Dubrana[1,2] ✉

DNA double-strand breaks (DSBs) must be repaired to ensure genome stability. Crucially, DSB-ends must be kept together for timely repair. In *Saccharomyces cerevisiae*, two pathways mediate DSB end-tethering. One employs the Mre11–Rad50–Xrs2 (MRX) complex to physically bridge DSB-ends. Another requires the conversion of DSB-ends into single-strand DNA (ssDNA) by Exo1, but the bridging proteins are unknown. We uncover that cohesin, its loader and Smc5/6 act with Exo1 to tether DSB-ends. Remarkably, cohesin specifically impaired in oligomerization fails to tether DSB-ends, revealing a function for cohesin oligomerization. In addition to the known importance of sister chromatid cohesion, microscopy-based microfluidic experiments unveil a role for cohesin in repair by ensuring DSB end-tethering. Altogether, our findings demonstrate that oligomerization of cohesin prevents DSB end-separation and promotes DSB repair, revealing a previously undescribed mode of action and role for cohesin in safeguarding genome integrity.

DNA double-strand breaks (DSBs) pose a substantial threat to genome stability, as they disrupt chromosome integrity. Repair mechanisms, such as non-homologous end joining (NHEJ) and homologous recombination, are essential for restoring chromosome continuity by directly rejoining DSB-ends or using a donor homologous template[1]. However, before repair processes can occur, it is imperative to bring DSB-ends together, a task unlikely to be achieved through passive diffusion[2]. Instead, active DSB end-tethering mechanisms have been identified, and represent a critical step in preventing joining or recombination events between unrelated chromosome loci.

The mechanisms that facilitate DSB end-tethering were initially characterized in the budding yeast *Saccharomyces cerevisiae*[3–5]. The MRX^{MRN} complex (Mre11–Rad50–Xrs2^{NBS1}) is rapidly recruited to DSB-ends and plays an early role in end-tethering[3,5,6]. MRN has been proposed to serve a similar function in humans, preventing translocations[7–9]. In yeast, MRX nuclease activity is dispensable for DSB end-tethering. On the other hand, the Zn-hook domain and ATPase activity of Rad50 are essential, suggesting a physical bridging mechanism by MRX dimers[3]. In contrast, during later stages of repair, DSB end-tethering requires Exo1 exonuclease activity to reveal single-stranded DNA (ssDNA)[4]. However, the proteins responsible for physical bridging of DSB-ends during these late stages of repair remain unidentified.

Recent theoretical research has proposed a role for DNA loop extrusion in the tethering of DSB-ends[2]. Loop extrusion, a property associated with structural maintenance of chromosomes (SMC) family complexes, has emerged as a conserved mechanism for folding the genome[10]. Among the various SMC complexes, cohesin (comprising Smc1, Smc3, Mcd1^{Scc1} and Scc3$^{STAG1/2}$) and the Smc5/6 complex are recruited to DNA-damage sites in both yeast and mammals[11–14]. In yeast, cohesin loading to DSBs involves a number of factors, including the cohesin loader Scc2/Scc4, Smc5/6 and DNA damage factors such as MRX, γH2A, Tel1^{ATM} and Mec1^{ATR} (refs. 13–17). DSBs also enrich cohesin throughout the genome[18–20], contributing to tightening of sister chromatid cohesion (SCC)[18,19,21–23], locally restricting homology search[24] and aiding in DNA-damage checkpoint establishment[20].

Given the involvement of cohesin and SMC5/6 in DSB response[25,26], cohesin's ability to bridge DNA molecules in vitro[27], and gross chromosomal rearrangements in cohesin and SMC5/6 mutants[14,28],

---

[1]UMR Stabilité Génétique Cellules Souches et Radiations, Université Paris Cité, INSERM, CEA, Fontenay-aux-Roses, France. [2]UMR Stabilité Génétique Cellules Souches et Radiations, Université Paris-Saclay, INSERM, CEA, Fontenay-aux-Roses, France. ✉e-mail: karine.dubrana@cea.fr

we hypothesized that cohesin and/or Smc5/6 play a critical role in DSB repair by maintaining proximity between DSB-ends.

In this Article we combine genetic and live-microscopy-based approaches to demonstrate a cohesin-dependent DSB end-tethering mechanism involving Exo1 and Smc5/6. Furthermore, we show that cohesin compacts DSB-adjacent chromatin, beyond the compaction observed in G2/M cells. We expose oligomerization as a key mechanism for both MRX- and cohesin-dependent tethering through both disruption of protein–protein interactions in response to hexanediol treatment, and genetic loss of function mutants. Specifically, disruption of cohesin oligomerization through mutation in the Mcd1^{SCC1} subunit maintains compaction in the vicinity of DSB, but prevents DSB end-tethering. Finally, our real-time microfluidic assay demonstrates that cohesin is essential for efficient repair of DSBs, through its end-tethering capacity.

Results

Cohesin tethers DSB-ends

To assess the requirement of cohesin in tethering DSB-ends, we developed a microscopy-based assay in which LacO and TetO repeats were positioned either side of the endogenous Ho endonuclease cleavage site of *Saccharomyces cerevisiae* (Fig. 1a; ref. 29). Targeted by LacI–mCherry and TetR–GFP fusion proteins, these arrays allow for visualization of the regions flanking the DSB site. DSBs were induced by galactose treatment, which triggers *GAL* promoter-controlled expression of the Ho endonuclease (Extended Data Fig. 1a). In individual cells, we distinguished tethering or separation of DSB-ends based on the distance between the spot centres being less than or greater than 400 nm (Fig. 1b). This threshold was established by quantifying spot separation in the absence of DNA DSBs, where less than 5% of wild-type (WT) cells exhibited spots exceeding 400-nm separation (Extended Data Fig. 1b). We confirmed the assay's sensitivity to detect previously described, early MRX- and late Exo1-dependent end-tethering pathways by imaging at 2 h and 4 h post-DSB induction. At 2 h post-DSB, WT and *exo1Δ* cells showed less than 10% separation, whereas cells lacking Mre11 displayed 31% separation (Fig. 1c and Extended Data Fig. 1c). At 4 h post-DSB, separation remained unchanged in WT cells but increased to 23% in *exo1Δ* cells. Importantly, double deletion of *EXO1* and *MRE11* led to a significant increase in end-separation compared to either single mutation, highlighting the presence of two DSB end-tethering pathways (Fig. 1d and Extended Data Fig. 1d).

To investigate cohesin in DSB end-tethering, we employed the auxin-induced degron (AID) system to deplete the Smc1 subunit[30]. Following a 1-h auxin incubation, Smc1 protein levels were substantially reduced and maintained at near undetectable levels for 4 h (Extended Data Fig. 2a). Depletion of Smc1 resulted in cells with separated sister chromatids (Fig. 1e) and impaired cell growth (Extended Data Fig. 2e), consistent with the essential role of cohesin in SCC. At 2 h post-DSB, a slight but significant increase in end-separation was observed (Fig. 1f). Strikingly, at 4 h post-DSB, ~30% of DSB-ends were untethered (Fig. 1f). To ensure that the increase in spot separation above 400 nm was due to the lack of DSB end-tethering and not due to the loss of cohesin-mediated chromatin folding, we quantified the percentage of cells with spots exceeding 400 nm upon Smc1 depletion in the absence of DSB. No significant increase in spot separation was observed when Smc1 was depleted in the absence of DSBs (Fig. 1f and Extended Data Fig. 1d), excluding an involvement of cohesin-mediated chromatin folding. Overall, these results reveal a cohesin requirement for DSB end-tethering.

Early cohesin tethering is independent of MRX and Exo1

Because both MRX and cohesin were required for early DSB tethering, we asked whether they act in the same pathway. Loss of Smc1 in *mre11Δ* cells significantly increased end-separation at 2 h post-DSB (Fig. 1g), suggesting that MRX and cohesin act in different pathways. Considering that Exo1 is not involved in early DSB tethering (Fig. 1c), our results suggest that, at 2 h post-DSB, cohesin acts independently of MRX and Exo1 to ensure DSB end-tethering.

Late cohesin tethering relies only on Exo1

At 4 h post-DSB, depleting cohesin in *mre11Δ* cells significantly increased end-separation (Fig. 1h), recapitulating the separation observed in *mre11Δ exo1Δ* cells (Fig. 1d). In contrast, depletion of Smc1 in *exo1Δ* cells did not further increase end-separation compared to *exo1Δ* cells (Fig. 1i). These findings suggest that cohesin functions with Exo1 to tether DSB-ends at 4 h post-DSB.

Altogether, our data indicate that cohesin supports DSB end-tethering at early and late time points through different pathways. Initially, cohesin tethering acts independently of the known MRX and Exo1 pathways, whereas later cohesin acts in the Exo1-dependent pathway.

Late DSB end-tethering requires de novo cohesin loading

Next, we interrogated whether cohesin present on chromosomes before DSB induction is sufficient for DSB end-tethering, or whether DSB-induced de novo cohesin loading is required. Accordingly, we arrested cells in G2/M phase using nocodazole, depleted Scc2 for 1 h to prevent de novo cohesin loading while maintaining pre-existing loops[31], and induced DSB (Fig. 2a and Extended Data Fig. 2b). Smc1 depletion in nocodazole blocked cells lacking Mre11 resulted in increased separation at 2 h post DSB (Fig. 2b and Extended Data Fig. 3a), as was the case in the absence of nocodazole (Fig. 1g). In contrast, we observed no increase in end-separation upon depletion of Scc2 in nocodazole-arrested *mre11Δ* cells after 2 h DSB, showing that cohesin de novo loading is not required to tether DSB-ends at early time points (Fig. 2b and Extended Data Fig. 3a). After 4 h DSB induction, DSB end-separation significantly increased upon Scc2 depletion, reaching a similar level to that observed in Smc1-depleted and *exo1Δ* cells under the same experimental settings (Fig. 2c and Extended Data Fig. 3b). These results indicate that preformed cohesin loops participate in DSB end-tethering early post-DSB induction, but are not sufficient later, when de novo loading of cohesin is necessary for DSB end-tethering.

DSB end-tethering does not require sister chromatid cohesion

Despite efficient cleavage of both sister chromatids in our assay (Extended Data Fig. 1a), which makes tethering of a cleaved chromatid by its sister unlikely, we aimed to confirm that DSB end-tethering was independent of SCC. In the absence of Cdc45, G1 cells progress to G2/M phase and load cohesin on chromosomes without firing replication origins and synthesizing sister chromatids[32] (Fig. 2d and Extended Data Figs. 2d,e and 4). Depletion of Cdc45 did not disrupt DSB end-tethering at 4 h post-DSB induction (Fig. 2e and Extended Data Fig. 3c), indicating that the presence of a sister chromatid is not essential for DSB end-tethering. Additional depletion of Smc1 resulted in increased DSB end-separation, reaching levels similar to those observed in cells depleted of Smc1 alone. This indicates that cohesin can tether DSB-ends even in the absence of DNA replication and a sister chromatid.

Late cohesin DSB end-tethering requires Smc5/6

Previous studies have shown the importance of Smc5/6 in enriching cohesin at DSBs[17]. Accordingly, we depleted Smc5 in our DSB end-tethering assay (Extended Data Fig. 2c,e). At 4 h post-DSB induction, Smc5 depletion resulted in a significant increase in DSB end-separation (Fig. 2f and Extended Data Fig. 3d). Simultaneous depletion of Smc5 and Smc1 did not increase end-separation beyond that observed upon Smc1 depletion alone, indicating that cohesin and Smc5/6 function in the same pathway to tether DSB-ends.

Together, these findings unveil a series of events that ultimately result in cohesin-dependent DSB end-tethering. Initially, preformed

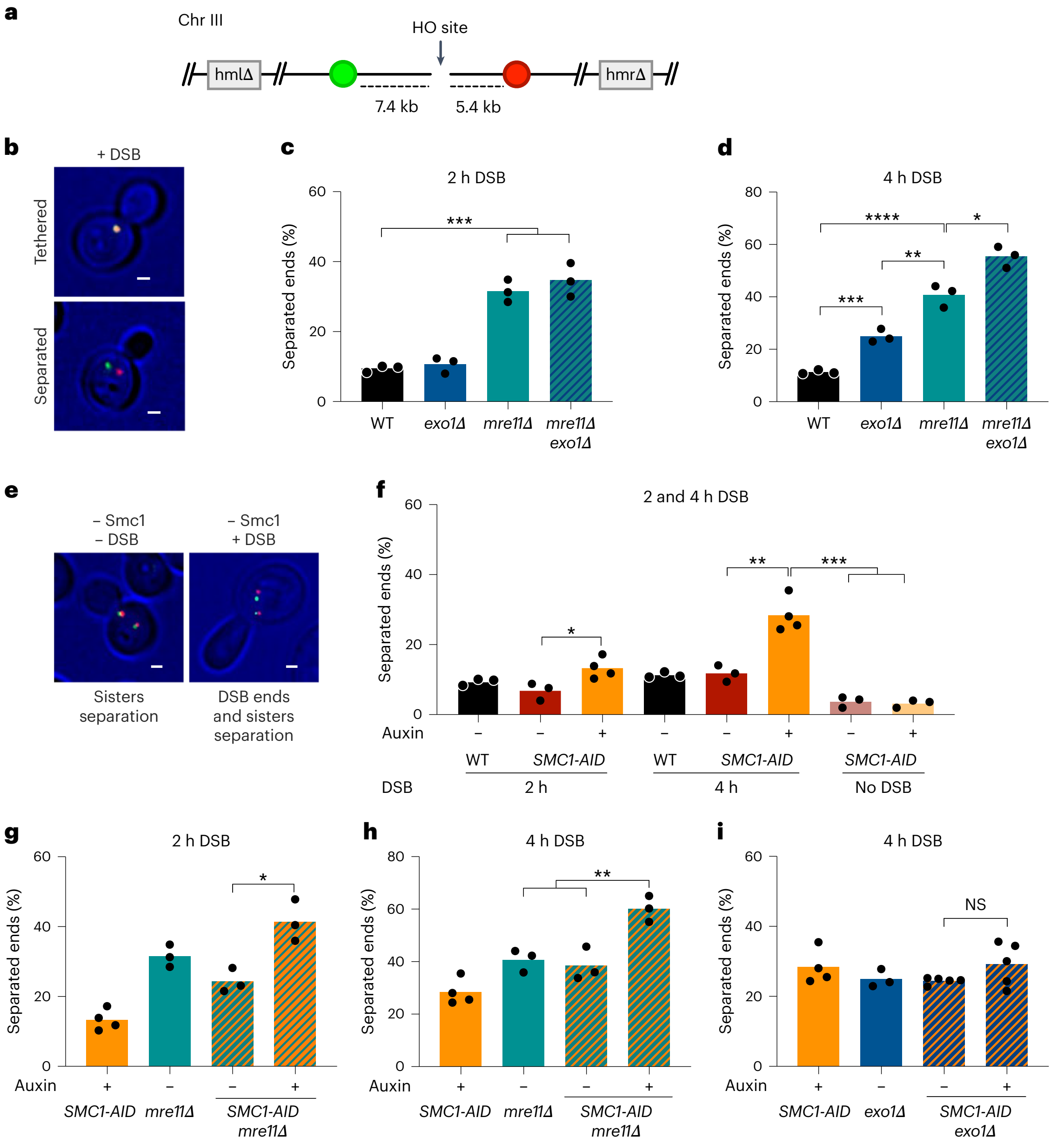

Fig. 1 | Cohesin tethers DSB-ends in the Exo1 pathway. a, A LacO/LacI–mCherry tag and a TetO/TetR–GFP tag were inserted at 5 and 7 kb from the Ho DSB site at the mating-type (MAT) locus, respectively. **b**, Example of cells with tethered or separated ends. The images are maximum intensity projections and representative of the independent experiments quantified in **c** and **d**. Signals are considered as separated when the distance between centres is more than 400 nm. Scale bars, 1 µm. **c**,**d**, Percentage of cells with separated ends in the indicated strains after 2 h (**c**) or 4 h (**d**) DSB induction. **e**, Examples of cells showing sister chromatid separation and DSB end-separation upon Smc1-AID auxin-mediated degradation in the absence or presence of DSB induction. The images are maximum intensity projections and are representative of the independent experiments quantified in **f**. Scale bars, 1 µm. **f**, Percentage of cells with separated ends in WT and SMC1-AID strains in the absence (−) or presence (+) of auxin after 2 h, 4 h or no DSB induction as indicated. **g**,**i**, Percentage of cells with separated ends in the indicated strains after 2 h (**g**) or 4 h (**i**) DSB induction. Data are presented as the mean of more than $n = 3$ independent experiments with $N \geq 150$ for each strain and condition (**c**,**d**,**f**–**i**). See source numerical data for detailed numbers. Overlaid black dots show the value of independent biological replicates. P values were calculated using a two-tailed unpaired t-test (*$P \leq 0.05$, **$P \leq 0.01$, ***$P \leq 0.001$, ****$P \leq 0.0001$, not significant (NS) $P > 0.05$). Numerical P values are provided in Supplementary Table 4. In **c**, WT versus *mre11Δ* $P = 0.0003$, WT versus *mre11Δ exo1Δ* $P = 0.0009$. In **d**, WT versus *exo1Δ* $P = 0.0009$, WT versus *mre11Δ* $P = 0.0003$, *exo1Δ* versus *mre11Δ* $P = 0.0053$, *mre11Δ* versus *mre11Δ exo1Δ* $P = 0.0126$. In **f**, 2 h *SMC1-AID* − auxin versus *SMC1-AID* + auxin $P = 0.0292$, 4 h *SMC1-AID* − auxin versus *SMC1-AID* + auxin $P = 0.0033$, 4 h *SMC1-AID* + auxin versus *SMC1-AID* − auxin no DSB $P = 0.0005$, 4 h *SMC1-AID* + auxin versus *SMC1-AID* + auxin no DSB $P = 0.0004$. In **g**, *mre11Δ SMC1-AID* − auxin versus *mre11Δ SMC1-AID* + auxin $P = 0.0128$. In **h**, *mre11Δ* versus *mre11Δ SMC1-AID* + auxin $P = 0.0068$, *mre11Δ SMC1-AID* − auxin versus *mre11Δ SMC1-AID* + auxin $P = 0.0095$. In **i**, *exo1Δ SMC1-AID* − auxin versus *exo1Δ SMC1-AID* + auxin $P = 0.1253$.

cohesin loops and binding of the MRX complex tethers DSB-ends. Later, an Exo1-dependent pathway comes into play with the recruitment and de novo loading of cohesin, facilitated by Scc2/4 and Smc5/6, actively participating in the tethering of DSB-ends within individual chromatids.

Cohesin orchestrates compaction of DSBs flanking chromatin

Cohesin has been shown to form DNA loops and we hypothesized that this activity could contribute to cohesin-dependent DSB end-tethering. To gain insights into the behaviour of cohesin in the chromatin surrounding DSBs, we modified our assay to investigate chromatin

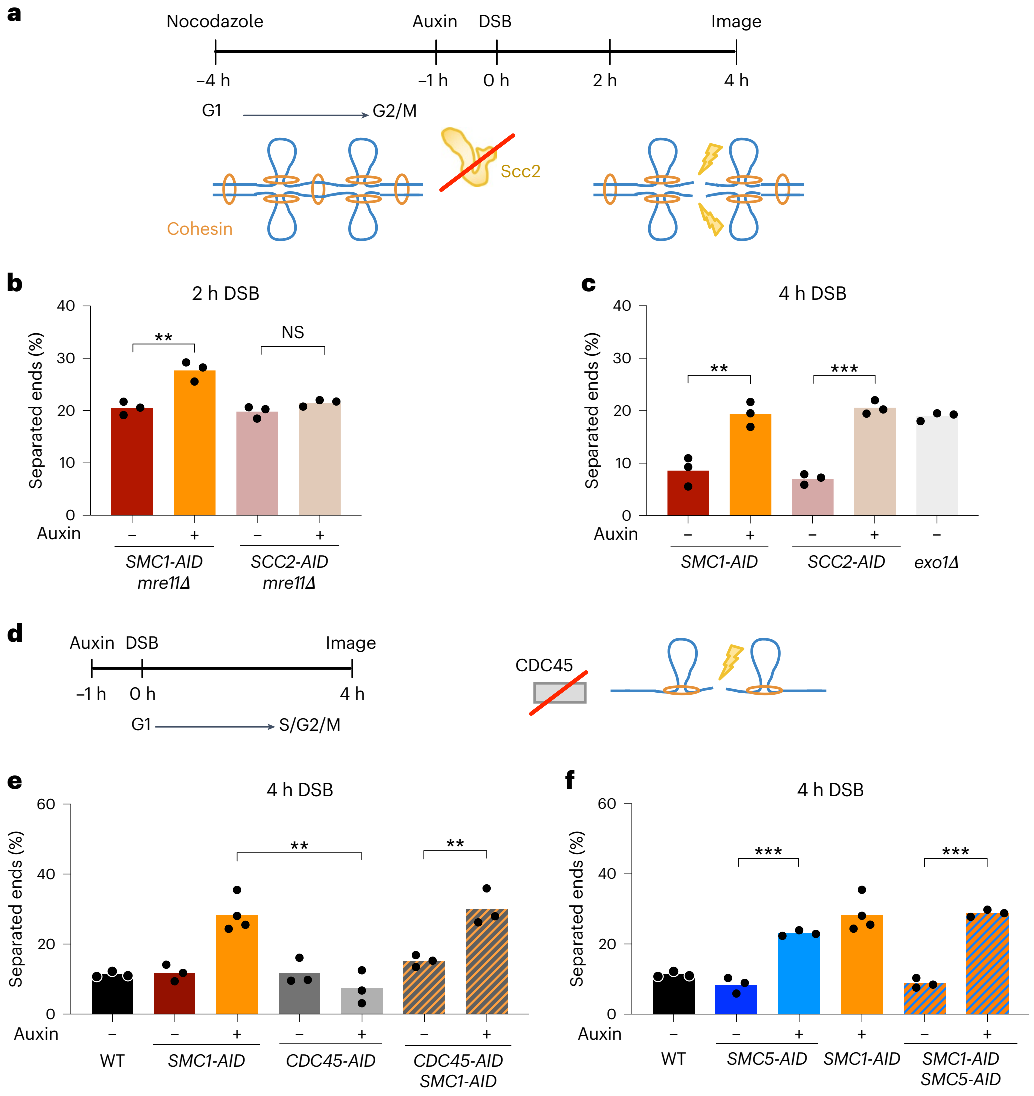

Fig. 2 | Cohesin DSB end-tethering requires de novo cohesin loading but not sister chromatid cohesion. **a**, Schematic representation of an assay to determine DSB end-tethering in the absence of de novo cohesin loading. DSBs were induced after cells were blocked in G2/M with nocodazole for 3 h, and incubated with auxin or ethanol for a further 1 h. **b**,**c**, Percentage of G2/M blocked cells with separated ends in the indicated strains after 2 (**b**) or 4 h (**c**) DSB induction. **d**, Schematic representation of the assay used in **e** to determine DSB end-tethering in the absence of replication. G1 arrested cultures were incubated with auxin or ethanol for 1 h before release in galactose and auxin containing medium. In the absence of Cdc45, cells advance through the cell cycle upon DSB induction, and load cohesin onto chromosomes without undergoing replication. **e**,**f**, Percentage of cells with separated ends in the indicated strains after 4 h DSB induction. Data are presented as the mean of more than three independent experiments with $N = 150$ for each strain and condition (**b**,**c**,**e**,**f**). See source numerical data for detailed numbers. Overlaid black dots show the values of independent biological replicates. P values were calculated using a two-tailed unpaired t-test (*$P \leq 0.05$, **$P \leq 0.01$, ***$P \leq 0.001$, ****$P \leq 0.0001$, NS $P > 0.05$). Numerical P values are provided in Supplementary Table 4. In **b**, *mre11Δ SMC1-AID* − auxin Noc versus *mre11Δ SMC1-AID* + auxin Noc $P = 0.0054$, *mre11Δ SCC2-AID* − auxin versus *mre11Δ SCC2-AID* + auxin $P = 0.0886$. In **c**, *SMC1-AID* + auxin Noc versus *SMC1-AID* − auxin Noc $P = 0.0068$. In **e**, *SMC1-AID* + auxin versus *CDC45-AID* + auxin $P = 0.0025$, *SMC1-AID CDC45-AID* − auxin versus *SMC1-AID CDC45-AID* + auxin $P = 0.0092$, *SCC2-AID* + auxin Noc versus *SCC2-AID* − auxin Noc $P = 0.0032$. In **f**, *SMC1-AID SMC5-AID* + auxin versus *SMC1-AID SMC5-AID* + auxin $P < 0.0001$, *SMC5-AID* + auxin versus *SMC5-AID* + auxin $P = 0.0004$.

compaction in a 48-kb region flanked by LacO–LacI–mCherry and TetO–TetR–GFP arrays, located 7 kb upstream of the DSB site (Fig. 3a). We measured the distance between these two signals in the presence or absence of DSB, to evaluate DSB-induced chromatin compaction. As the occurrence of a DSB triggers the DNA-damage checkpoint and a G2/M cell-cycle arrest, we treated all cells with nocodazole to ensure a fair comparison between DSB and no-DSB conditions (Fig. 3b).

We first examined the impact of cohesin chromatin folding in G2/M-arrested cells with no DSB. Cohesin depletion significantly increased the distribution of distances between spots (Fig. 3c and Extended Data Fig. 5a), showing that our assay detects the previously reported cohesin-dependent compaction of chromatin[33,34]. Following 4 h of DSB induction, we detected a significant reduction in spot distances compared to the no-DSB condition, indicative of a compaction of the DSB-flanking chromatin (Fig. 3d; black versus red). DSB-induced compaction was abolished upon depletion of Smc1, demonstrating that cohesin compacts DSB flanking sequences (Fig. 3d, orange and Extended Data Fig. 5b).

Pds5 facilitates DSB end-tethering but not genome compaction

If loop formation were at the basis of DSB end-tethering, the latter should be challenged by modulating loop expansion and turnover. To explore this, we tested the role of Pds5, a key factor in cohesin loop

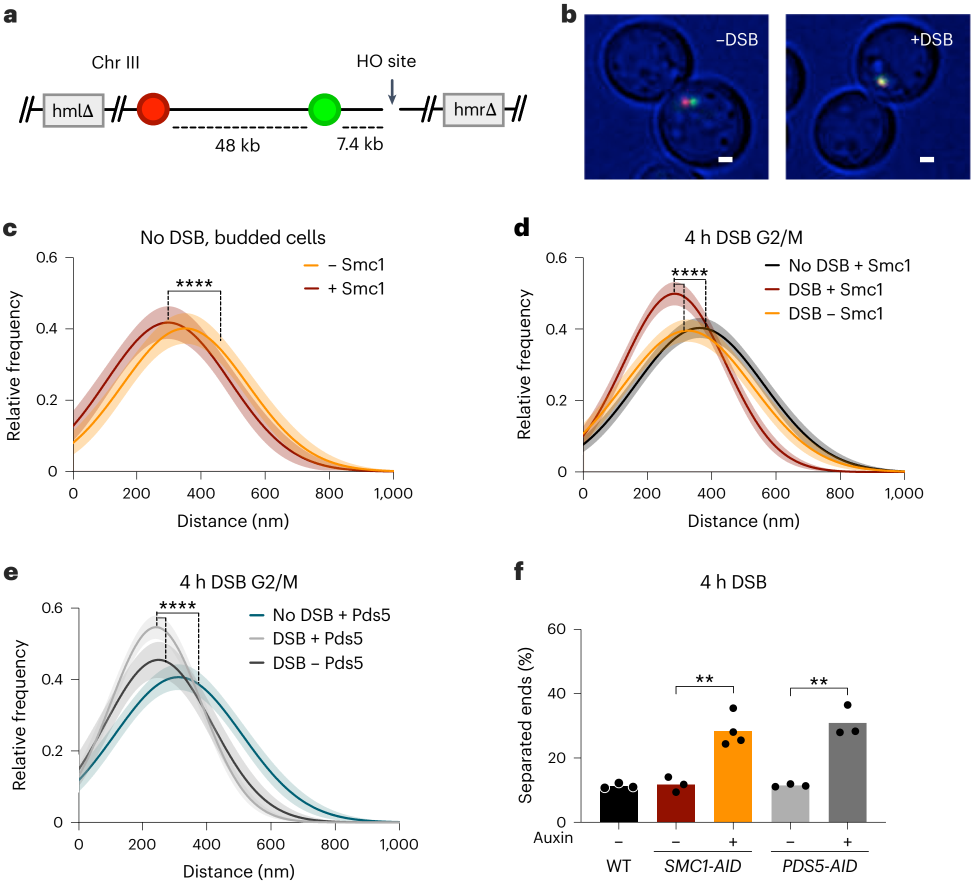

Fig. 3 | Cohesin compacts DSBs flanking chromatin. **a**, LacO/LacI–mCherry tags and a TetO/TetR–GFP tag inserted at 7 and 55 kb from the Ho DSB site at the MAT locus, respectively. **b**, Representative images illustrating spot separation in the presence and absence of DSBs for the experiments quantified in **c**–**e**. Scale bars, 1 µm. **c**, Relative frequency of distances between the two tags in *SMC1-AID*-tagged budded cells treated with ethanol (+Smc1) or auxin (−Smc1). **d**, Relative frequency of distances between the two tags in nocodazole-arrested *SMC1-AID*-tagged cells treated with ethanol (+Smc1) or auxin (−Smc1) after 4 h and no DSB. **e**, Relative frequency of distances measured between the two tags in nocodazole-arrested *PDS5-AID*-tagged cells treated with ethanol (+Pds5) or auxin (−Pds5) after 4 h or no DSB induction. Shaded areas in **c**–**e** represent Gaussian fitting (solid line) of $n = 3$ biological replicates with $N \geq 300$ for each strain and condition, and a confidence interval of 95%. P values were calculated on the distance distribution using a two-tailed unpaired Mann–Whitney test. **f**, Percentage of cells with separated ends in the indicated strains after 4 h DSB induction. Overlaid black dots show the values of independent biological replicates. P values were calculated using a two-tailed unpaired t-test. Data are presented as the mean of more than three independent experiments with $N \geq 150$ for each strain and condition (**c**–**f**). See source numerical data for detailed numbers (*$P \leq 0.05$, **$P \leq 0.01$, ***$P \leq 0.001$, ****$P \leq 0.0001$, NS $P > 0.05$). Numerical P values are presented in Supplementary Table 4. In **c**, −*SMC1* versus +*SMC1* $P < 0.0001$. In **d**, no DSB + Smc1 versus DSB + Smc1 $P < 0.0001$, DSB − Smc1 versus DSB + Smc1 $P < 0.0001$. In **e**, no DSB + Pds5 versus DSB + Pds5 $P < 0.0001$, DSB − Pds5 versus DSB + Pds5 $P < 0.0001$. In **f**, 4 h *SMC1-AID* − auxin versus *SMC1-AID* + auxin $P = 0.0033$, 4 h PDS5-AID − auxin versus PDS5-AID + auxin $P = 0.0022$.

regulation. Pds5 depletion weakens loop boundaries, reduces defined chromosome contacts/loops, and generates much longer loops in regions such as those near centromeres[35,36]. DSB-induced chromatin compaction, although slightly affected, still occurred in the absence of Pds5 (Fig. 3e and Extended Data Fig. 5c–e). In contrast, Pds5 depletion increased end-separation at 4 h post-DSB, mimicking the effects of cohesin depletion (Fig. 3e and Extended Data Fig. 5f). These results imply that either the loops formed in the absence of Pds5 were not sufficient to support the function of cohesin in DSB end-tethering, or that cohesin tethers DSB-ends independently of loop formation, through another mechanism requiring Pds5. A recent study revealed an essential role of Pds5 in the oligomerization of multiple cohesin complexes[37], opening the door for a role of Pds5-dependent cohesin oligomerization in DSB end-tethering.

Cohesin and MRX tethering use weak hydrophobic interactions

To investigate whether protein–protein interactions and cohesin oligomerization participate in DSB end-tethering, we used the aliphatic alcohol 1,6-hexanediol. Hexanediol has been instrumental in studying the liquid-phase separation and oligomerization properties of various proteins, including cohesin and proteins involved in the DNA-damage response[38,39]. Notably, it disrupts MRX and Rad52 foci (Extended Data Fig. 6a–d).

Treatment of cells with hexanediol 10 min before imaging at 2 h post-DSB, when tethering mostly relies on MRX, increased end-separation independently of Smc1 presence (Fig. 4a–c). Moreover, end-separation was not increased by hexanediol in the absence of Mre11 alone. These results suggest a role for weak hydrophobic interactions in MRX-dependent tethering. Strikingly, hexanediol-treated *mre11Δ* cells do not exhibit the separation levels observed in Smc1-depleted *mre11Δ* cells, with or without hexanediol treatment (Figs. 4c, 1g and Extended Data Fig. 6e). This finding aligns with a recent in vivo study in *S. cerevisiae* that demonstrated the resistance of a subset of topologically important cohesins to hexanediol treatment[38]. As hexanediol is known to disrupt protein–protein interactions, this further supports our finding that an Exo1-independent population of cohesin can tether DSB-ends that are formed within a cohesin loop (Fig. 1g).

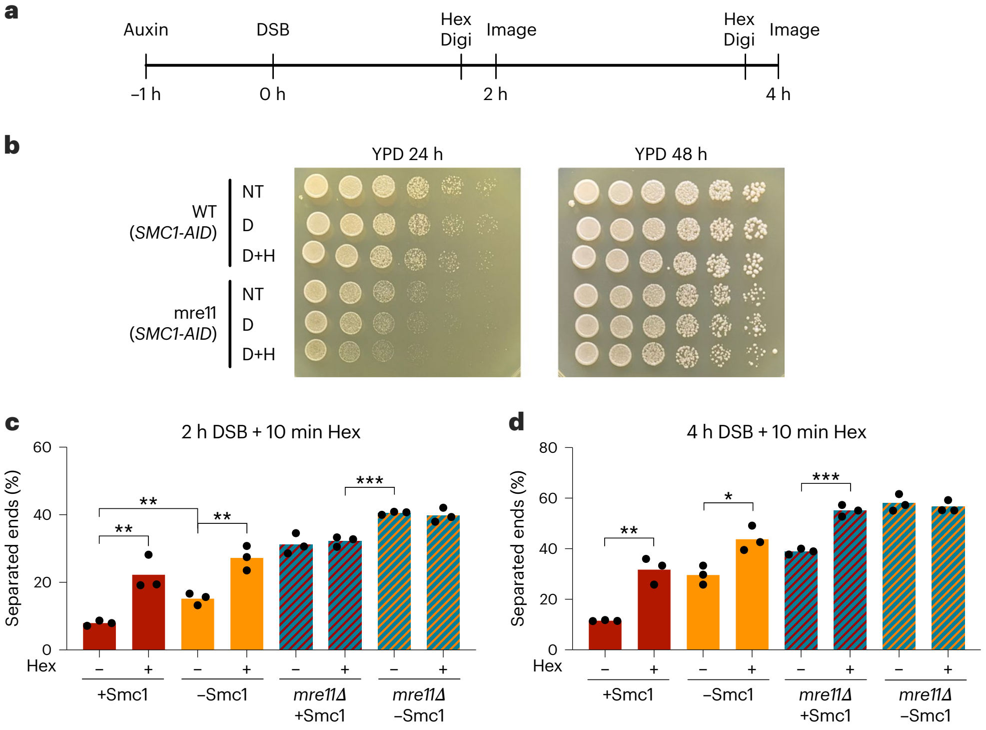

Fig. 4 | DSB-ends tethering by MRX or cohesin is sensitive to hexanediol treatment. **a**, Schematic representation of the assay to test DSB end-tethering sensitivity to hexanediol (Hex). **b**, Drop assay of strains plated on YPD after no treatment (NT), 10 min digitonin (D) or 10 min digitonin + hexanediol (D + H) treatment, incubated for 24 and 48 h at 30 °C. **c**,**d**, Percentage of cells with separated ends in the indicated strains treated with auxin or ethanol, and for 10 min with digitonin (−) or digitonin and 1,6-hexanediol (+), after 2 h (**c**) or 4 h (**d**) DSB induction. Data are presented as the mean of more than three independent experiments with $N \geq 150$ for each strain and condition (**c**,**d**). See source numerical data for detailed numbers. Overlaid black dots show the values of independent biological replicates. P values were calculated using a two-tailed unpaired t-test (*$P \leq 0.05$, **$P \leq 0.01$, ***$P \leq 0.001$, ****$P \leq 0.0001$, NS $P > 0.05$). Numerical P values are presented in Supplementary Table 4. In **c**, −Hex + Smc1 versus −Hex + Smc1 $P = 0.0027$, −Hex − Smc1 versus +Hex − Smc1 $P = 0.0170$, +Hex *mre11Δ* + Smc1 versus −Hex *mre11Δ* − Smc1 $P = 0.0004$. In **d**, −Hex + Smc1 versus −Hex + Smc1 $P = 0.0027$, −Hex − Smc1 versus +Hex − Smc1 $P = 0.0170$, +Hex *mre11Δ* + Smc1 versus −Hex *mre11Δ* − Smc1 $P = 0.0004$.

At 4 h post-DSB, hexanediol-treated control cells also exhibited untethering (Fig. 4d and Extended Data Fig. 6f). In line with hexanediol disruption of MRX-dependent tethering at 2 h, hexanediol and Smc1 depletion have additive effects at 4 h. In contrast to the 2-h time point, hexanediol increased end-separation in *mre11Δ* cells to levels comparable to cells depleted for both Smc1 and Mre11, suggesting disruption of cohesin-dependent DSB end-tethering (Fig. 4d). These results indicate that protein–protein interactions play a key role in DSB end-tethering by both MRX and cohesin pathways. Because hexanediol might affect proteins acting in these pathways other than MRX and cohesin, we aimed to directly test the relevance of oligomerization using specific mutants.

MRX has been shown to form oligomers in vitro, and disruption of these oligomers by a mutation of the hydrophobic interaction patch within the Rad50 head domain (*rad50lo* mutant[40]) led to the disappearance of DSB-dependent Mre11 foci in vivo. Because hexanediol also disrupts Mre11-GFP foci formation in our strain background (Extended Data Fig. 6c,d), we introduced this mutation in our tethering system. The rad50lo mutant protein is expressed at nearly WT levels in our strain background and remains proficient for NHEJ (Extended Data Fig. 7a,b). Notably, NHEJ is significantly increased in the *rad50lo* mutant compared to WT cells, consistent with the decreased resection previously described in this mutant[40]. Complementation of *rad50Δ* cells with *rad50lo* did not affect end-separation levels compared to WT at 2 h post-DSB (Fig. 5a and Extended Data Fig. 7c). Therefore, disrupting Rad50 head oligomerization is not sufficient to impair DSB end-tethering. However, the disruption of the MRX-dependent pathway of DSB end-tethering by hexanediol suggests that MRX may achieve this through oligomerization using other interfaces such as the Zn-hook[3], or that oligomerization of other proteins acting with MRX is required (Fig. 5b).

The cohesin subunit Mcd1 has been identified as a mediator of cohesin oligomerization, and a five-amino-acid insertion at Q266 in its regulation of cohesion and condensation (ROCC) domain has been shown to abolish cohesin oligomerization in vivo[37,41]. To test the role of cohesin oligomerization in DSB end-tethering, we complemented *MCD1-AID* cells with the *mcd1-Q266* mutant in both our compaction and end-tethering strains (Extended Data Fig. 8a,b). In contrast to cells depleted for Mcd1, *mcd1Q266* mutant cells did not exhibit separated DSB-ends at 2 h, indicating that early DSB end-tethering does not rely on cohesin oligomerization (Fig. 5c and Extended Data Fig. 8c), and probably relies on preformed loops (Fig. 5b). Critically, *mcd1Q266* mutants exhibited strong DSB-dependent genome compaction at 4 h (Fig. 5d,e and Extended data Fig. 8d–f), indicating that cohesin is recruited to DSB sites and able to form chromatin loops. However, unlike complementation with *MCD1*, *mcd1Q266* failed to restore DSB end-tethering to WT-like levels (Fig. 5f and Extended Data Fig. 8g), confirming the importance of cohesin oligomerization in DSB end-tethering (Fig. 5g).

Cohesin assists DSB repair by homology-directed mechanisms

Having identified cohesin's role in DSB end-tethering, we questioned its importance for repair. We took advantage of our tethering system, which contains direct homologous repeats flanking the inserted LacO and TetO arrays (Fig. 6a). Following DSB induction and resection initiation, progressive formation of ssDNA away from the DSB causes loss of the dsDNA substrate that is necessary for the binding of the

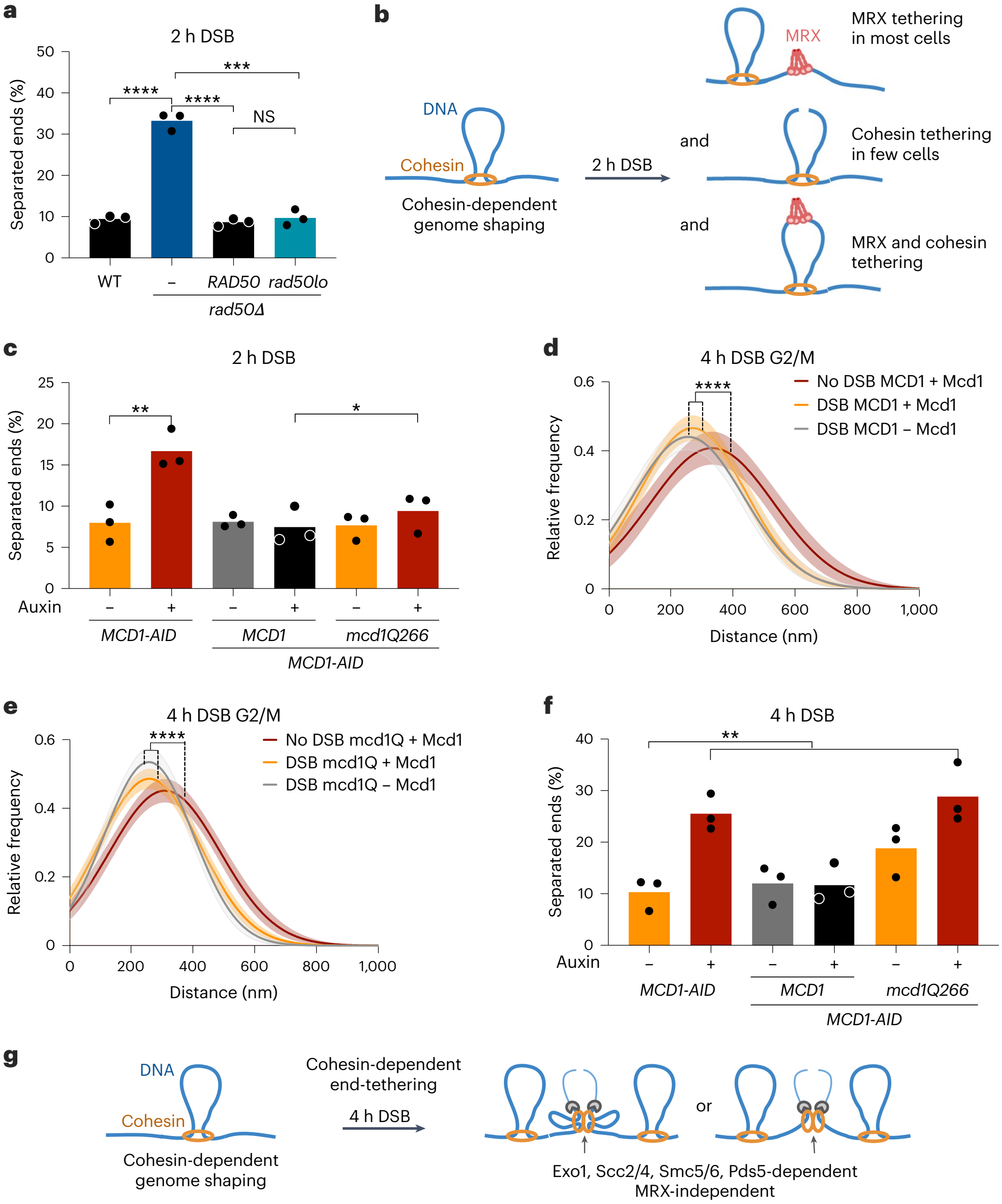

Fig. 5 | DSB-ends are tethered by MRX or cohesin oligomerization. **a**, Percentage of cells with separated ends in WT, *rad50Δ* and *rad50Δ* cells complemented with *RAD50* or *rad50-lo*, after 2 h of DSB induction. **b**, Model for 2-h cohesin-mediated end-tethering. DSB-ends are primarily tethered by MRX assisted by cohesin-mediated loops. Cohesin tethering is independent of oligomerization and de novo loading. **c**, Percentage of cells with separated ends in *MCD1-AID*, and *MCD1-AID* strains complemented with *MCD1* or *mcd1Q266*, in the absence (−) or presence (+) of auxin, after 2 h of DSB induction. Data are presented as the mean of more than three independent experiments with $N \geq 50$ for each strain and condition. See source numerical data for detailed numbers. Overlaid black dots show the value of independent biological replicates. *P* values were calculated using a two-tailed unpaired *t*-test. **d**,**e**, Relative frequency of distances measured between two tags separated by 45 kb in *MCD11-AID*-tagged strains complemented with *MCD1* (**d**) or *mcd1Q266* (**e**), treated with ethanol or auxin and nocodazole after 4 h DSB induction. Shaded areas in **d** and **e** indicate the 95% confidence intervals of the Gaussian fitting (solid line) of three independent experiments, with $N \geq 300$ for each strain and condition. *P* values were calculated on the distance distribution using a two-tailed unpaired Mann–Whitney test (**d**,**e**). **f**, Percentage of cells with separated ends in *MCD1-AID*, and *MCD1-AID* strains complemented with *MCD1* or *mcd1-Q266*, in the absence (−) or presence (+) of auxin, after 4 h of DSB induction. Data are presented as the mean of more than three independent experiments with $N \geq 50$ for each strain and condition. See source numerical data for detailed numbers. Overlaid black dots show the value of independent biological replicates. *P* values were calculated using a two-tailed unpaired *t*-test. **g**, Model for 4-h cohesin-mediated end-tethering. Cohesin mediates DSB end-tethering by oligomerization in a MRX-independent but Exo1-, Scc2-, Smc5/6- and Pds5-dependent manner (*$P \leq 0.05$, **$P \leq 0.01$, ***$P \leq 0.001$, ****$P \leq 0.0001$, NS $P > 0.05$). Numerical *P* values are provided in Supplementary Table 4. In **a**, WT versus *rad50Δ* $P < 0.0001$, *rad50Δ* versus *RAD50* $P < 0.0001$, *rad50Δ* versus *rad50lo* $P = 0.0001$, *RAD50* versus *rad50lo* $P = 0.4411$. In **c**, *MCD1-AID* − auxin versus *MCD1-AID* + auxin $P = 0.0100$. In **d**, no DSB *MCD1* + Mcd1 versus DSB *MCD1* + Mcd1 $P < 0.0001$, no DSB *MCD1* + Mcd1 versus DSB *MCD1* − Mcd1 $P < 0.0001$. In **e**, no DSB *mcd1Q* + Mcd1 versus DSB *mcd1Q* + Mcd1 $P < 0.0001$, no DSB *mcd1Q* + Mcd1 versus DSB *mcd1Q* − Mcd1 $P < 0.0001$. In **f**, *MCD1-AID* − auxin versus *MCD1-AID* + auxin $P = 0.0050$, *MCD1-AID MCD1* + auxin versus *MCD1-AID mcd1Q266* + auxin $P = 0.0127$.

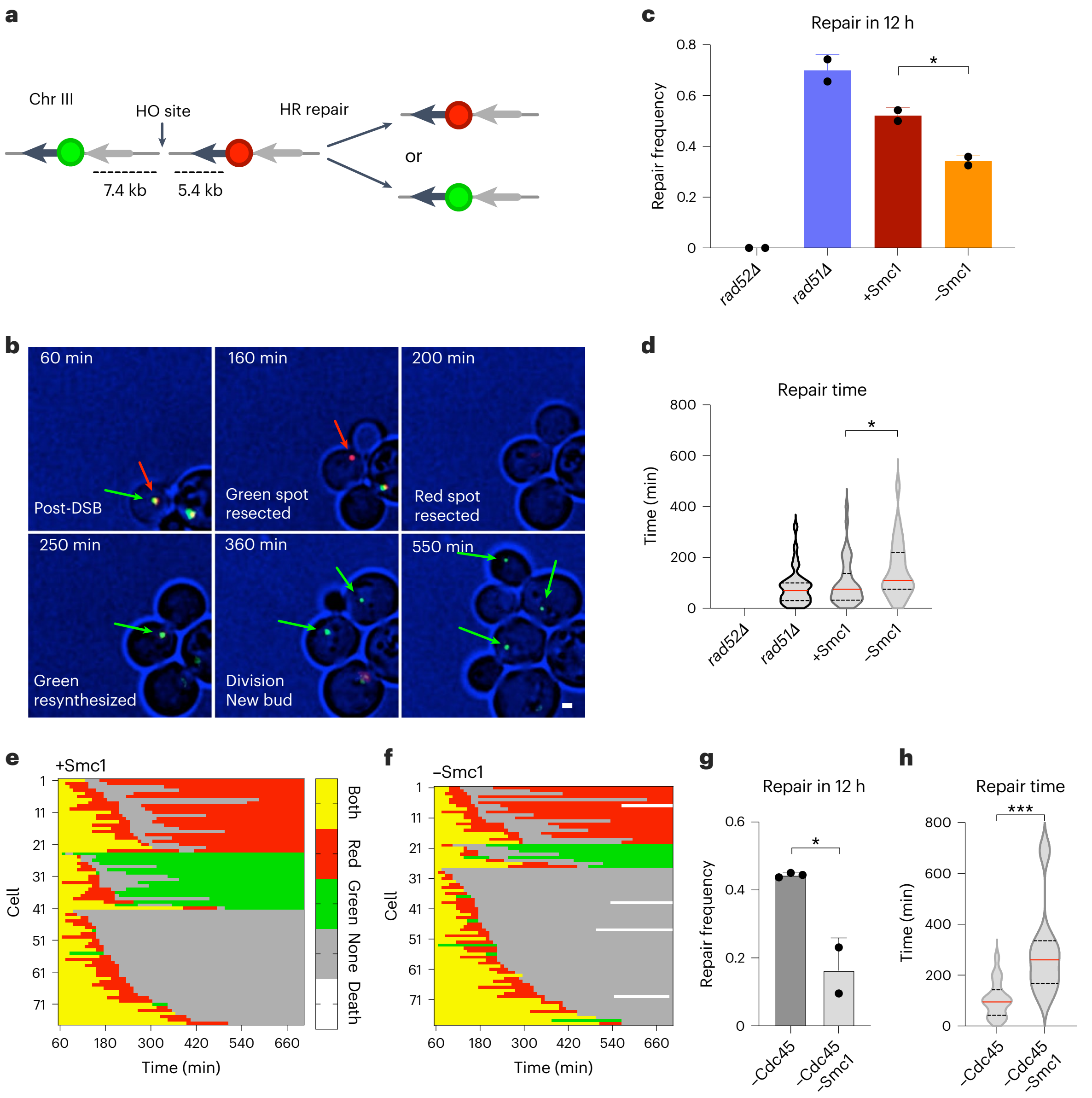

Fig. 6 | Cohesin is required for efficient DNA DSB repair. a, Schematic representation of repair events after resection and disappearance of the spots followed by resynthesis of one spot. Black and grey arrows show direct repeats used for homologous recombination. **b**, Sequence of images showing the disappearance of both spots upon resection, and the reappearance of a green spot that is propagated to daughter cells at each division. The time post DSB induction is indicated on each frame. This sequence is representative of the repair events quantified in **c**–**h**. Scale bar, 1 µm. **c**, Relative frequency of repair events corresponding to the resynthesis of a spot in *rad52*Δ, *rad51*Δ and *SMC1-AID* strains treated with ethanol (+Smc1) or auxin (−Smc1). Data are presented as means ± s.d. *P* values were calculated using a two-tailed unpaired *t*-test. **d**, Time taken for a spot to reappear, in *rad52*Δ, *rad51*Δ and *SMC1-AID* strains treated with ethanol (+Smc1) or auxin (−Smc1). The red line represents the median, and quartiles are represented by dashed lines. *P* values were calculated using a two-tailed unpaired Mann–Whitney test. Data are representative of $N = 61$ (rad52*Δ*), $N = 54$ (rad51), $N = 77$ (+Smc1) and $N = 79$ (−Smc1) cells from $n = 2$ independent experiments (**c**,**d**). **e**,**f**, Spot characteristics of +Smc1 (**e**) and −Smc1 (**f**), individual cells imaged every 10 min over 12 h after DNA DSB induction. Lines represent individual cell lineages, and each segment a time point. Colours indicate the presence of both spots (yellow), a red spot only (red), a green spot only (green) or no spots (grey). Data are representative of $N = 77$ (+Smc1) and $N = 79$ (−Smc1) cells from $n = 2$ independent experiments (**e**,**f**). **g**, Relative frequency of repair events corresponding to the resynthesis of a spot in the indicated strains treated with auxin. Cells in G1 phase upon induction were imaged. Data are presented as means ± s.d. *P* values were calculated using a two-tailed unpaired *t*-test. **h**, Time for a spot to reappear in the indicated strains treated with auxin. Cells in G1 phase upon induction were imaged. The red line represents the median, and quartiles are represented by dashed lines. *P* values were calculated using a two-tailed unpaired Mann–Whitney test. Data are representative of $N = 45$ (−Cdc45) and $N = 47$ (−Cdc45 − Smc1) cells from $n = 3$ (−Cdc45) and $n = 2$ (−Cdc45 − Smc1) independent experiments (**g**,**h**) ($^{*}P \leq 0.05$, $^{**}P \leq 0.01$, $^{***}P \leq 0.001$, $^{****}P \leq 0.0001$, NS $P > 0.05$). Numerical *P* values are provided in Supplementary Table 4. In **c**, +Smc1 versus −Smc1 $P = 0.0224$. In **d**, +Smc1 versus −Smc1 $P = 0.0307$. In **g**, −Cdc45 versus −Cdc45 − Smc1 $P = 0.0116$. In **h**, −Cdc45 versus −Cdc45 − Smc1 $P = 0.0004$.

LacI–mCherry and TetR–GFP fusion proteins, leading to the gradual disappearance of fluorescent signals. Resection also unmasks the direct homologous repeats, which can anneal and be used to resynthesize the broken DNA strand. This restores chromosome continuity but results in loss of the genetic material that previously separated the homologous repeats used for repair. Following resynthesis, either the red or green signal reappears, depending on the repeats used for repair (Fig. 6a,b). Following repair, cells are released from the DNA-damage checkpoint and proceed through cell division (Fig. 6b and Supplementary Videos 1–4).

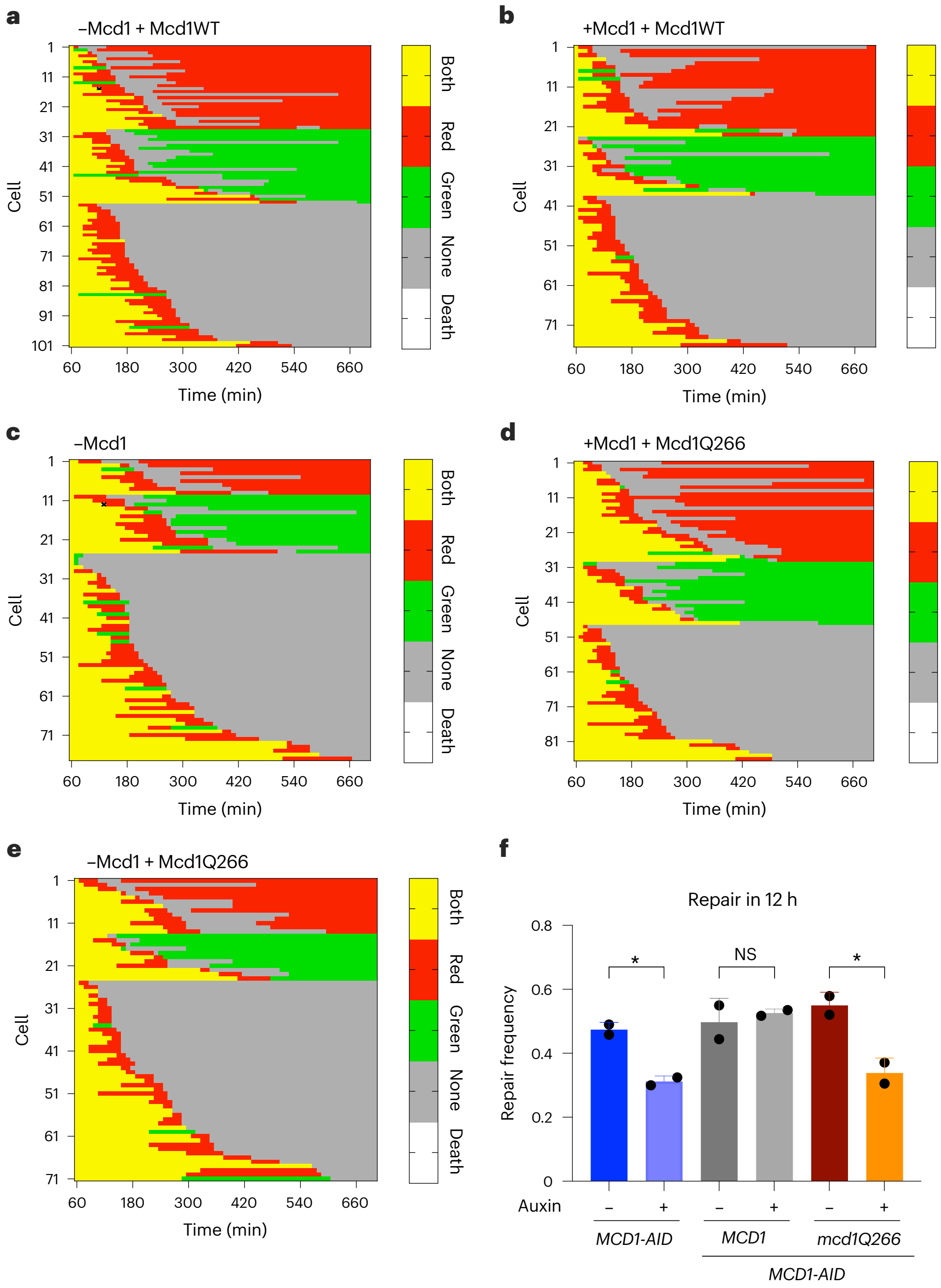

Fig. 7 | Cohesin oligomerization is required for efficient DNA DSB repair. **a**–**e**, Spot characteristics in *MCD1-AID*, and *MCD1-AID* strains complemented with nothing (**c**), *MCD1* (**a**,**b**) or *mcd1-Q266* (**d**,**e**), in the absence (+Mcd1) or presence (−Mcd1) of auxin for individual cells imaged every 10 min during a period of 12 h after DNA DSB induction. **f**, Relative frequency of repair events corresponding to the resynthesis of a spot in the indicated strains treated with auxin (+) or ethanol (−). Error bars represent s.d. *P* values were calculated using a two-tailed unpaired *t*-test. Data are representative of $N = 101$ (−Mcd1 + Mcd1WT), $N = 76$ (+Mcd1 + Mcd1WT), $N = 77$ (−Mcd1), $N = 86$ (+Mcd1 + Mcd1Q266) and $N = 71$ (−Mcd1 + Mcd1Q266) cells from $n = 2$ independent experiments (**a**–**f**) (*$P \leq 0.05$, **$P \leq 0.01$, ***$P \leq 0.001$, ****$P \leq 0.0001$, NS $P > 0.05$). Numerical *P* values are provided in Supplementary Table 4. In **f**, *MCD1-AID* − auxin versus *MCD1-AID* + auxin $P = 0.0149$, *MCD1 MCD1-AID* − auxin versus *MCD1 MCD1-AID* + auxin $P = 0.6439$, *mcd1Q266 MCD1-AID* − auxin versus *mcd1Q266 MCD1-AID* + auxin $P = 0.0406$.

To assess repair events, we employed a microfluidics system to follow individual cells and image each fluorescent signal over a 12-h period after DSB induction. To validate our assay, we imaged cells lacking *RAD52*, which is essential for all homology-directed repair (HDR) events. In the absence of Rad52, no instances of spot reappearance were observed (Fig. 6c and Extended Data Fig. 9a). Conversely, the loss of Rad51, which impedes gene conversion and promotes single-strand annealing (SSA), led to an increase in repair events compared to the WT-like condition (*SMC1-AID* without auxin; Fig. 6c,e and Extended Data Fig. 9b), as previously reported[42,43]. This result suggests that inhibiting gene conversion, and favouring repair by SSA, leads to more detectable repair events in this assay, with unaltered repair kinetics compared to the WT-like condition (Fig. 6d). In contrast, Smc1 depletion resulted in a significant reduction in repair frequency, with delayed repair kinetics (Fig. 6c–f). This decrease in repair frequency was not caused by a resection defect (Extended Data Fig. 9c). To separate the dependence of repair events on SCC and DSB end-tethering, we employed Cdc45 depletion. Strikingly, repair still occurred upon

Cdc45 depletion, whereas simultaneous depletion with Smc1 resulted in a severe decrease in repair frequency and kinetics compared to cells depleted of Cdc45 alone (Fig. 6g,h and Extended Data Fig. 9d–f). This result indicates that cohesin is necessary for DSB repair beyond its role in SCC. To specifically test the contribution of cohesin-dependent DSB end-tethering, we measured repair in the *mcd1Q266* mutant. Unlike complementation with *MCD1*, which exhibited WT repair levels, *mcd1Q266* cells exhibited decreased repair comparable to that observed upon Mcd1 depletion (Fig. 7a–f). Altogether, these results demonstrate that the specific function of cohesin in DSB end-tethering is essential for efficient repair between DSB-ends.

Discussion

Cohesin enrichment at DSBs has long been known[11–13], with early studies highlighting the importance of cohesin for survival after DNA damage-inducing radiation[11,13,44]. Recent observations suggest that loop extrusion at DNA DSBs helps establish DNA-damage response-related chromatin modifications[20], which ultimately organize DSBs into microdomains[45]. Moreover, SCC, which is increased in response to DSB[18,19,21–23], prevents promiscuous repair events with distant loci[24,28].

In addition to these functions, we reveal a DSB end-tethering role for cohesin. Cohesin's first contribution, early after DSB formation, is independent of MRX and Exo1 and probably relies on cohesin-dependent genome looping (Fig. 5c), as predicted by recent theoretical work[2]. In most cells, tethering is ensured by the MRX complex, probably independently of cohesin, as suggested by the additive end-tethering defect observed in the absence of both Mre11 and cohesin. However, we cannot exclude that cohesin loops or chromatin folding contribute to keeping ends close before MRX binding, improving the efficiency of MRX tethering without being absolutely required.

Later, cohesin DSB end-tethering requires de novo cohesin loading, acts in cooperation with Exo1 and Smc5/6, is independent of SCC and loop formation, and relies on cohesin oligomerization (Fig. 5g). Importantly, our data provide a biological function to the recently described cohesin oligomerization mechanism[37,38] that is independent of cohesin's canonical roles in SCC and loop extrusion.

Our results support the existence of two populations of DSB-bound cohesin with separable functions (chromatin compaction and DSB end-tethering), through different modes of action (loop formation and oligomerization). One population of cohesin acts in a Pds5- and oligomerization-independent manner and compacts DSB-adjacent chromatin. This compaction may participate in DSB signalling though a loop extrusion-mediated spreading of histone H2AX phosphorylation[20]. A second population requires Pds5 and cohesin oligomerization, and tethers DSB-ends. What distinguishes loop-forming cohesin from DSB end-tethering cohesin, beyond the capacity to form oligomers, is unknown. However, that DSB end-tethering cohesin acts independently of MRX, which has been implicated in cohesin enrichment at DSBs[12,15], suggests a different mode of recruitment to DSB-ends.

Our data support a role for Scc2-, Smc5/6- and Exo1-mediated ssDNA formation in recruiting or stabilizing DSB end-tethering cohesin. Scc2 and Smc5/6 were previously implicated in cohesin recruitment to DSB, but the formation of ssDNA by Exo1 is specifically required for cohesin-dependent DSB end-tethering. Given that dsDNA-bound cohesin can capture ssDNA[46], the formation of ssDNA may directly assist cohesin recruitment. Bridging dsDNA with ssDNA could also be sufficient for DSB end-tethering. Alternatively, cohesin recruitment may occur independently of ssDNA, which could instead mediate the recruitment of Smc5/6. Indeed, Smc5/6 interacts with ssDNA through its hinge domain[47,48], and stably associates with ss–dsDNA junctions[48,49]. Beyond recruiting tethering cohesin, Smc5/6 could also participate in DSB end-tethering through post-translational modification of proteins in the cohesin pathway. Indeed, Smc5/6 contains small ubiquitin-like modifier (SUMO) and ubiquitin ligase activities mediated by the Nse2/Mms21 and Nse1 subunits, respectively. The SUMO ligase activity of Smc5/6 targets numerous proteins implicated in genome organization, DNA replication and DNA repair[50]. Notably, substrates of Nse2/Mms21-mediated SUMOylation include subunits of the cohesin complex. Among these, the SUMOylation of Mcd1 is triggered by DSB induction and is required for DNA-damage-induced cohesion[17]. Given that interaction between SUMOylated proteins can lead to the formation of large protein aggregates[51], SUMOylation of Mcd1 by Smc5/6 could participate in cohesin oligomerization and DSB tethering.

Our results, revealing cohesin's role in DSB end-tethering, contrast with a previous report of a Hi-C approach suggesting that cohesin is dispensable for contacts between both sides of a DSB[24]. One plausible explanation for this discrepancy is rooted in the technologies used. Single-cell live-microscopy allows for detection of DSB-induced compaction beyond G2/M chromosome folding, and cohesin-dependent loss of end-tethering, both appearing below the detection threshold of the population-wide Hi-C approach[24].

We also demonstrate that loss of Rad50 head oligomerization observed in vitro is not sufficient to disrupt MRX end-tethering in vivo. MRX oligomerization via both the Rad50 heads and coiled coils has been described in both yeast and humans[40,52]. Disruption of DSB end-tethering of the MRX pathway by hexanediol treatment suggests a crucial contribution of oligomerization in this process. Hexanediol could disrupt oligomerization of the MRX complex via interfaces other than the Rad50 heads, such as the Zn-hook[3], or affect oligomerization of other complexes contributing to early DSB end-tethering, such as Nej1/Lif1[29].

Our results suggest that oligomerization of SMC complexes is a conserved and functionally relevant mechanism for maintaining genome integrity in response to DNA damage. Interestingly, hexanediol treatment disrupted MRX foci in response to DSBs, suggesting MRX at DSBs may form condensates. Although cohesin does not form detectable foci in response to DSBs in yeast, it has been shown to form phase separation condensates in vitro[38]. Thus, the relevance of phase separation in DSB end-tethering should be investigated using single-molecule microscopy.

Given the prevalence of chromosome translocations in cancer, and the role of DSB induction in cohesin-sensitive developmental processes such as V(D)J recombination[53], our study gives further insights into how SMC complex dysregulation may lead to disease in the human population.

Online content

Any methods, additional references, Nature Portfolio reporting summaries, source data, extended data, supplementary information, acknowledgements, peer review information; details of author contributions and competing interests; and statements of data and code availability are available at https://doi.org/10.1038/s41556-024-01552-2.

References

1. Bordelet, H. & Dubrana, K. Keep moving and stay in a good shape to find your homologous recombination partner. *Curr. Genet.* **65**, 29–39 (2019).
2. Yang, J. H., Brandão, H. B. & Hansen, A. S. DNA double-strand break end synapsis by DNA loop extrusion. *Nat. Commun.* **14**, 1913 (2023).
3. Lobachev, K., Vitriol, E., Stemple, J., Resnick, M. A. & Bloom, K. Chromosome fragmentation after induction of a double-strand break is an active process prevented by the RMX repair complex. *Curr. Biol.* **14**, 2107–2112 (2004).
4. Nakai, W., Westmoreland, J., Yeh, E., Bloom, K. & Resnick, M. A. Chromosome integrity at a double-strand break requires exonuclease 1 and MRX. *DNA Repair* **10**, 102–110 (2011).
5. Lee, K., Zhang, Y. & Lee, S. E. *Saccharomyces cerevisiae* ATM orthologue suppresses break-induced chromosome translocations. *Nature* **454**, 543–546 (2008).

6. Oh, J., Lee, S. J., Rothstein, R. & Symington, L. S. Xrs2 and Tel1 independently contribute to MR-mediated DNA tethering and replisome stability. *Cell Rep.* **25**, 1681–1692.e4 (2018).
7. De Jager, M. et al. Human Rad50/Mre11 is a flexible complex that can tether DNA ends. *Mol. Cell* **8**, 1129–1135 (2001).
8. van der Linden, E., Sanchez, H., Kinoshita, E., Kanaar, R. & Wyman, C. RAD50 and NBS1 form a stable complex functional in DNA binding and tethering. *Nucleic Acids Res.* **37**, 1580–1588 (2009).
9. Roukos, V. et al. Spatial dynamics of chromosome translocations in living cells. *Science* **341**, 660–664 (2013).
10. Davidson, I. F. & Peters, J.-M. Genome folding through loop extrusion by SMC complexes. *Nat. Rev. Mol. Cell Biol.* **22**, 445–464 (2021).
11. Sjögren, C. & Nasmyth, K. Sister chromatid cohesion is required for postreplicative double-strand break repair in *Saccharomyces cerevisiae*. *Curr. Biol.* **11**, 991–995 (2001).
12. Kim, J.-S., Krasieva, T. B., LaMorte, V., Taylor, A. M. R. & Yokomori, K. Specific recruitment of human cohesin to laser-induced DNA damage. *J. Biol. Chem.* **277**, 45149–45153 (2002).
13. Ström, L., Lindroos, H. B., Shirahige, K. & Sjögren, C. Postreplicative recruitment of cohesin to double-strand breaks is required for DNA repair. *Mol. Cell* **16**, 1003–1015 (2004).
14. De Piccoli, G. et al. Smc5–Smc6 mediate DNA double-strand-break repair by promoting sister-chromatid recombination. *Nat. Cell Biol.* **8**, 1032–1034 (2006).
15. Ünal, E. et al. DNA damage response pathway uses histone modification to assemble a double-strand break-specific cohesin domain. *Mol. Cell* **16**, 991–1002 (2004).
16. Lindroos, B. H. et al. Chromosomal association of the Smc5/6 complex reveals that it functions in differently regulated pathways. *Mol. Cell* **22**, 755–767 (2006).
17. McAleenan, A. et al. SUMOylation of the α-kleisin subunit of cohesin is required for DNA damage-induced cohesion. *Curr. Biol.* **22**, 1564–1575 (2012).
18. Ström, L. et al. Postreplicative formation of cohesion is required for repair and induced by a single DNA break. *Science* **317**, 242–245 (2007).
19. Ünal, E., Heidinger-Pauli, J. M. & Koshland, D. DNA double-strand breaks trigger genome-wide sister-chromatid cohesion through Eco1 (Ctf7). *Science* **317**, 245–248 (2007).
20. Arnould, C. et al. Loop extrusion as a mechanism for formation of DNA damage repair foci. *Nature* **590**, 660–665 (2021).
21. Heidinger-Pauli, J. M., Ünal, E. & Koshland, D. Distinct targets of the Eco1 acetyltransferase modulate cohesion in S phase and in response to DNA damage. *Mol. Cell* **34**, 311–321 (2009).
22. Dodson, H. & Morrison, C. G. Increased sister chromatid cohesion and DNA damage response factor localization at an enzyme-induced DNA double-strand break in vertebrate cells. *Nucleic Acids Res.* **37**, 6054–6063 (2009).
23. Kim, B.-J. et al. Genome-wide reinforcement of cohesin binding at pre-existing cohesin sites in response to ionizing radiation in human cells. *J. Biol. Chem.* **285**, 22784–22792 (2010).
24. Piazza, A. et al. Cohesin regulates homology search during recombinational DNA repair. *Nat. Cell Biol.* **23**, 1176–1186 (2021).
25. Phipps, J. & Dubrana, K. DNA repair in space and time: safeguarding the genome with the cohesin complex. *Genes* **13**, 198 (2022).
26. Cost, G. J. & Cozzarelli, N. R. Smc5p promotes faithful chromosome transmission and DNA repair in *Saccharomyces cerevisiae*. *Genetics* **172**, 2185–2200 (2006).
27. Gutierrez-Escribano, P. et al. A conserved ATP- and Scc2/4-dependent activity for cohesin in tethering DNA molecules. *Sci. Adv.* **5**, eaay6804 (2019).
28. Gelot, C. et al. The cohesin complex prevents the end joining of distant DNA double-strand ends. *Mol. Cell* **61**, 15–26 (2016).
29. Mojumdar, A. et al. Nej1 interacts with Mre11 to regulate tethering and Dna2 binding at DNA double-strand breaks. *Cell Rep.* **28**, 1564–1573.e3 (2019).
30. Brocas, C., Ducrot, C. & Dubrana, K. Degradation of *S. cerevisiae* cohesin with the auxin-inducible degron system. *Methods Mol. Biol. Clifton NJ* **2004**, 17–24 (2019).
31. Bastié, N. et al. Smc3 acetylation, Pds5 and Scc2 control the translocase activity that establishes cohesin dependent chromatin loops. *Nat. Struct. Mol. Biol.* **29**, 575–585 (2022).
32. Tercero, J. A., Labib, K. & Diffley, J. F. DNA synthesis at individual replication forks requires the essential initiation factor Cdc45p. *EMBO J.* **19**, 2082–2093 (2000).
33. Schalbetter, S. A. et al. SMC complexes differentially compact mitotic chromosomes according to genomic context. *Nat. Cell Biol.* **19**, 1071–1080 (2017).
34. Lazar-Stefanita, L. et al. Cohesins and condensins orchestrate the 4D dynamics of yeast chromosomes during the cell cycle. *EMBO J.* **36**, 2684–2697 (2017).
35. Costantino, L., Hsieh, T.-H. S., Lamothe, R., Darzacq, X. & Koshland, D. Cohesin residency determines chromatin loop patterns. *eLife* **9**, e59889 (2020).
36. Dauban, L. et al. Regulation of cohesin-mediated chromosome folding by Eco1 and other partners. *Mol. Cell* **77**, 1279–1293.e4 (2020).
37. Xiang, S. & Koshland, D. Cohesin architecture and clustering in vivo. *eLife* **10**, e62243 (2021).
38. Ryu, J.-K. et al. Bridging-induced phase separation induced by cohesin SMC protein complexes. *Sci. Adv.* **7**, eabe5905 (2021).
39. Miné-Hattab, J. et al. Single molecule microscopy reveals key physical features of repair foci in living cells. *eLife* **10**, e60577 (2021).
40. Kissling, V. M. et al. Mre11-Rad50 oligomerization promotes DNA double-strand break repair. *Nat. Commun.* **13**, 2374 (2022).
41. Eng, T., Guacci, V. & Koshland, D. ROCC, a conserved region in cohesin's Mcd1 subunit, is essential for the proper regulation of the maintenance of cohesion and establishment of condensation. *Mol. Biol. Cell* **25**, 2351–2364 (2014).
42. Cerqueira, P. G. et al. *Saccharomyces cerevisiae* DNA polymerase IV overcomes Rad51 inhibition of DNA polymerase δ in Rad52-mediated direct-repeat recombination. *Nucleic Acids Res* **51**, 5547–5564 (2023).
43. Manthey, G. M. & Bailis, A. M. Rad51 inhibits translocation formation by non-conservative homologous recombination in *Saccharomyces cerevisiae*. *PLoS ONE* **5**, e11889 (2010).
44. Kong, X. et al. Distinct functions of human cohesin-SA1 and cohesin-SA2 in double-strand break repair. *Mol. Cell. Biol.* **34**, 685–698 (2014).
45. Fu, J. et al. ATM-ESCO2-SMC3 axis promotes 53BP1 recruitment in response to DNA damage and safeguards genome integrity by stabilizing cohesin complex. *Nucleic Acids Res* **51**, 7376–7391 (2023).
46. Murayama, Y., Samora, C. P., Kurokawa, Y., Iwasaki, H. & Uhlmann, F. Establishment of DNA-DNA interactions by the cohesin ring. *Cell* **172**, 465–477.e15 (2018).
47. Roy, M.-A. & D'Amours, D. DNA-binding properties of Smc6, a core component of the Smc5-6 DNA repair complex. *Biochem. Biophys. Res. Commun.* **416**, 80–85 (2011).
48. Tanasie, N.-L., Gutiérrez-Escribano, P., Jaklin, S., Aragon, L. & Stigler, J. Stabilization of DNA fork junctions by Smc5/6 complexes revealed by single-molecule imaging. *Cell Rep.* **41**, 111778 (2022).
49. Chang, J. T.-H. et al. Smc5/6's multifaceted DNA binding capacities stabilize branched DNA structures. *Nat. Commun.* **13**, 7179 (2022).
50. Roy, S., Adhikary, H. & D'Amours, D. The SMC5/6 complex: folding chromosomes back into shape when genomes take a break. *Nucleic Acids Res* **52**, 2112–2129 (2024).

51. Yau, T.-Y., Sander, W., Eidson, C. & Courey, A. J. SUMO interacting motifs: structure and function. *Cells* **10**, 2825 (2021).
52. Rotheneder, M. et al. Cryo-EM structure of the Mre11-Rad50-Nbs1 complex reveals the molecular mechanism of scaffolding functions. *Mol. Cell* **83**, 167–185.e9 (2023).
53. Peters, J.-M. How DNA loop extrusion mediated by cohesin enables V(D)J recombination. *Curr. Opin. Cell Biol.* **70**, 75–83 (2021).

Methods

Strains and plasmids

The yeast strains used in this study are derivative of JKM179, JKM139[54] or yKD809[29], and were generated by polymerase chain reaction (PCR) gene targeting, plasmid transformation or cross (Supplementary Tables 1 and 2).

Media and growth conditions

Yeast strains were grown at 30 °C in glucose rich yeast extract–peptone–dextrose (YPD) medium, with appropriate antibiotic, or in synthetic medium (SD) lacking the appropriate amino acid. YPLGg medium containing 2% lactate, 3% glycerol and 0.05% glucose was used for DNA DSB induction, by addition of galactose (final concentration of 2%), to overnight (ON) cultures with an optical density at 600 nm (OD_{600}) of 0.4–0.8, as in ref. 55. Conditional protein knockdown was achieved in AID-tagged strains by the addition of 3-indoleacetic acid (IAA) in EtOH to a final concentration of 2 mM (ref. 30) for 1 h before DSB induction by galactose addition (final concentration of 2%) for 2 or 4 h. 1,6-hexanediol treatment (final concentration of 10%) with 10 µg ml^{-1} digitonin was performed for 10 min before imaging.

Microscopy

Live-cell images were acquired using a wide-field inverted microscope (Leica DMI-6000B) equipped with adaptive focus control to eliminate Z drift, a ×100/1.4-NA immersion objective with a Prior NanoScanZ Nanopositioning Piezo Z Stage System, a complementary metal–oxide–semiconductor (CMOS) camera (ORCA-Flash4.0; Hamamatsu) and a solid-state light source (Spec-traX, Lumencore). The system was piloted by MetaMorph software (Molecular Device, v7.10.5). Images were acquired at indicated time points after DSB induction. Nineteen focal steps of 0.20 µm were acquired sequentially for green fluorescent protein (GFP) and mCherry with an exposure time of 50 ms using solid-state 475- and 575-nm diodes and appropriate filters (GFP-mCherry filter; excitation: double BP, 450–490/550–590 nm and dichroic double BP 500–550/600–665 nm; Chroma Technology Corp.). Images were processed using Fiji ImageJ software (National Institutes of Health, ImageJ2 v2.14.0/1.54f). Three-dimensional (3D) images were converted to 2D projections, from which *xy* coordinates of the most intense pixels were extracted. Distance analysis between the closest fluorescent signals in the mCherry and GFP channels was performed using an Rstudio script. When sister chromatids were separated, taking into account only the smallest distance underestimated separation. All images shown are maximal *z* projections of *z*-stack images.

Microscopy in microfluidic plates

CellASIC ONIX microfluidic plates (Y04C-02; MilliporeSigma) were used for long-duration movies. Ho was induced in YPLGg cultures with an OD_{600} of 0.5 by addition of galactose to a final concentration of 2%, and incubation at 30 °C for 30 min. After break induction, cultures were loaded into the microfluidic plate. The remaining culture was centrifuged at 900*g* for 3 min, and the conditioned medium was loaded into the microfluidic plate for flow over the cells for the duration of the experiment. After loading the plate, cell positions were defined, and images were acquired every 10 min for up to 24 h. Nineteen focal steps of 0.20 µm were acquired sequentially for GFP and mCherry, with an exposure time of 30 ms, using solid-state 475- and 575-nm diodes and appropriate filters (GFP-mCherry filter; excitation: double BP, 450–490/550–590 nm and dichroic double BP 500–550/600–665 nm; Chroma Technology Corp.). A single bright-field image on one focal plane was acquired at each time point with an exposure of 10 ms. For Cdc45 depleted strains, cells were loaded into the microfluidic plate immediately following galactose addition, and cells that were in G1 before DSB induction were imaged.

Monitoring DSB efficiency

Cells were grown in 2 ml of YPD ON. Cultures were then diluted in YPLGg, and grown to an OD_{600} of 0.5–0.8, then incubated with 2 mM IAA or EtOH for 1 h. Ho expression was then induced by addition of galactose to a final concentration of 2%. At 0, 1, 2, 4 and 6 h post DSB induction, ~4×10^7 cells were collected by 900*g* centrifugation for 5 min. DNA was extracted from cell pellets by Winston preparation. Samples were analysed by quantitative PCR with primers 1 kb upstream of the Ho site to analyse resection (200 nM), flanking the Ho site to determine DSB efficiency (450 nM) or targeting the OGG1 reference gene (200 nM). Supplementary Table 3 provides the primer sequences. Reactions were performed as in ref. 56. Each sample and no-template controls were run in triplicate, and reaction specificity was determined by melt curve analysis. Relative quantitation of resection and DSB efficiency reactions was achieved using the comparative Ct method[57].

Western blot

Auxin-induced protein degradation of AID-containing strains was confirmed by western blot analysis[30]. Cells were grown in 2 ml of YPD ON. Cultures were then diluted in YPLGg, and grown to an OD_{600} of 0.5–0.8, and incubated with 2 mM IAA or EtOH for 1, 2 and 4 h. Approximately 4 OD_{600} of cells were collected by centrifugation at 900*g* for 5 min. Cells were washed in dH_2O, and collected by centrifugation at 900*g* for 5 min. The supernatant was removed, and the cell pellets were frozen at −80 °C. Whole-cell extracts were prepared from the cell pellets using a standard trichloroacetic acid extraction protocol, then suspended in Laemmli buffer. Protein concentrations were determined by Bradford assay, and samples prepared for sodium dodecyl sulfate polyacrylamide gel electrophoresis (SDS–PAGE) by 5-min incubation at 90 °C. A 20-µg sample was migrated at 100 V for 1 h on 10% SDS polyacrylamide gels in standard running buffer. Nitrocellulose membrane transfer was performed using the iBlot transfer apparatus according to the manufacturer's guidelines (Thermo Fisher). Membranes were washed with TBS-T, revealed by Ponceau staining, and blocked with 5% milk TBS-T for 1 h. The membranes were then incubated at room temperature with mouse primary anti-myc (1:1,000; anti-myc tag antibody (9E10) Abcam ab32), anti-Flag (1:4,000; ANTI-FLAG M2 antibody Sigma-Aldrich F3165), anti-Rad50 (1:1,000; PA5-32176 Invitrogen) and fluorescent secondary antibodies (1:10,000; goat anti-rabbit immunoglobulin G (IgG) (H + L) highly cross-adsorbed secondary antibody, Alexa Fluor Plus 800, Invitrogen A32735; goat anti-mouse IgG (H + L) highly cross-adsorbed secondary antibody, Alexa Fluor Plus 680, Invitrogen A32729; and goat anti-mouse IgG (H + L) highly cross-adsorbed secondary antibody, Alexa Fluor Plus 800 Invitrogen A32730) in 5% milk TBS-T for 1 h each. The membranes were developed by fluorescence using an Odyssey Clx system (LI-COR).

Flow cytometry

First, 0.5 OD_{600} of cells were fixed in ethanol (70%) and stored at −20 °C. Cells were pelleted, washed, and then incubated in sodium citrate pH 7.4, 50 mM with 0.25 mg ml^{-1} RNAseA for 1 h at 50 °C. Proteinase K was added to a final concentration of 2 mg ml^{-1}, followed by incubation for a further 1 h at 50 °C. Cells were pelleted, then stained in a pH 7.4 50 mM sodium citrate solution containing 1 µM SYTOX Green nucleic acid stain (Invitrogen, S7020). Cells were sonicated, and flow cytometry was performed on a Novocyte cytometer (ACEA Bioscience). The data were analysed using FlowJo software (BD Biosciences, v10.10).

Statistics and reproducibility

For all experiments, no statistical method was used to predetermine sample size. Sample sizes are provided in the numerical source data or in the figure legends. The imaging data were excluded from analysis when a poor signal did not allow analysis. The experiments were not randomized. The investigators were not blinded to allocation during the experiments and outcome assessment. Quantifications and statistical analyses were done using GraphPad Prism v10.3.1. For the end-tethering assay, at least three independent experiments, each analysing more than 50 cells, were performed for each genotype, and statistical significance was determined by a two-tailed unpaired *t*-test. For the compaction measurements, distance data for at least 100 cells were sorted into 200-nm bins, and the bins of three independent experiments were fitted with a Gaussian curve using Prism software, with shaded areas representing a confidence interval of 95%. Statistical significance was determined on the distance distribution using a two-tailed unpaired Mann–Whitney test. Exact cell and biological replicates numbers are indicated in the figure legends or numerical source data. The statistical tests used are indicated in the figure legends and in Supplementary Table 4. *P* values that were <0.05 were considered statistically significant. Statistical differences are indicated by an asterisk ($^*P \leq 0.05$, $^{**}P \leq 0.01$, $^{***}P \leq 0.001$, $^{****}P \leq 0.0001$, and non-significance by NS, $P > 0.05$). Numerical *P* values are indicated in the respective figure legends and listed in Supplementary Table 4.

Reporting summary

Further information on research design is available in the Nature Portfolio Reporting Summary linked to this Article.

Data availability

All data supporting the findings in this study are available in the main text or the Supplementary Information (numerical source data and unprocessed blot images). Strains and raw images quantified but not shown in the Article are available upon request. Source data are provided with this paper.

References

54. Lee, S. E. et al. *Saccharomyces* Ku70, mre11/rad50 and RPA proteins regulate adaptation to G2/M arrest after DNA damage. *Cell* **94**, 399–409 (1998).
55. Bordelet, H. et al. Sir3 heterochromatin protein promotes non-homologous end joining by direct inhibition of Sae2. *EMBO J.* **41**, e108813 (2022).
56. Batté, A. et al. Recombination at subtelomeres is regulated by physical distance, double-strand break resection and chromatin status. *EMBO J.* **36**, 2609–2625 (2017).
57. Livak, K. J. & Schmittgen, T. D. Analysis of relative gene expression data using real-time quantitative PCR and the 2(-Delta Delta C(T)) Method. *Methods San Diego Calif.* **25**, 402–408 (2001).

Acknowledgements

We thank F. Uhlmann, S. Marcand, A. Quinet, A. Campalans, P. Radicella and P. Bertrand for critical reading of this manuscript, and members of the Dubrana and Marcand laboratories for stimulating discussions. We thank D. Koshland and M. Peter for sharing plasmids and strains. This research was supported by the European Research Council under the European Community's Seventh Framework Programme (FP7/2007 2013/European Research Council grant agreement 281287) to K.D., Fondation ARC pour la Recherche sur le Cancer (PJA-20191209432) to K.D. and the CEA Radiation Biology and Impulsion programmes, EDF, to K.D. J.P. was supported by a fellowship from the CEA.

Author contributions

J.P., M.T., C.D., C.B. and R.C. performed experiments. K.D. designed and supervised the entire project with the help of M.T. and J.P. K.D. and J.P. analysed the data, assembled the figures and wrote the manuscript, with critical input from the other authors.

Competing interests

The authors declare no competing interests.

Additional information

Extended data is available for this paper at https://doi.org/10.1038/s41556-024-01552-2.

Supplementary information The online version contains supplementary material available at https://doi.org/10.1038/s41556-024-01552-2.

Correspondence and requests for materials should be addressed to Karine Dubrana.

Peer review information *Nature Cell Biology* thanks Douglas Koshland and the other, anonymous, reviewer(s) for their contribution to the peer review of this work. Peer reviewer reports are available.

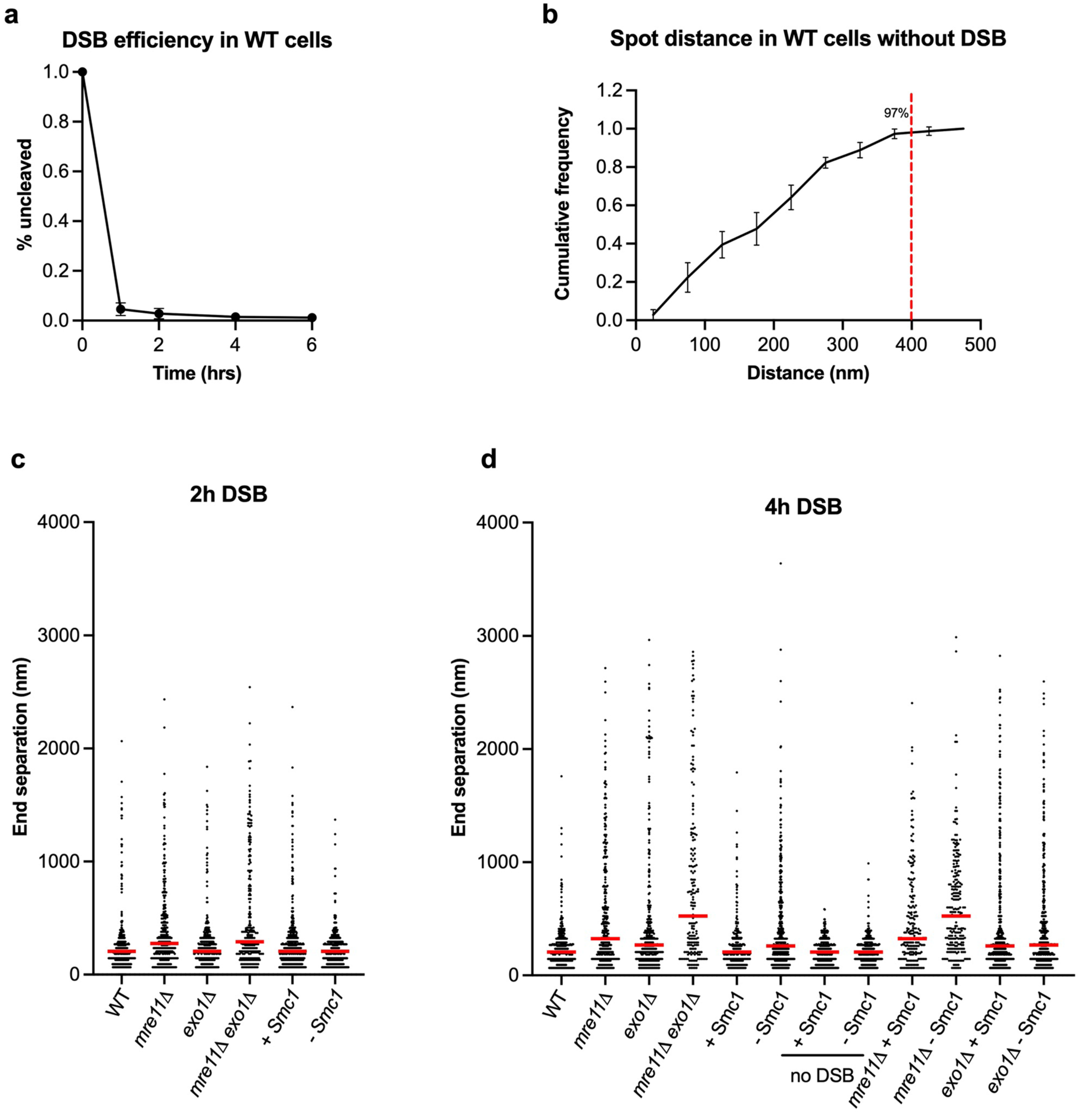

Extended Data Fig. 1 | End separation threshold definition and control of DSB efficiency. a, Measure of DSB efficiency by qPCR detection of the Ho cleavage site in WT cells at 0, 1, 2, 4 and 6 hours after DSB induction. Data are mean ± s.d. of 3 biological replicates. **b**, Cumulative distance between LacI–mCherry and TetR–GFP signals in exponential WT cells without DNA DSB induction. Red line indicates 400 nm threshold, which 97% of distances are under. Data are mean ± s.d. of 3 biological replicates. **c**, **d**, Scatter dot plots of end separation at 2 h and 4 h DSB corresponding to the pool of measurements of biological replicates presented in Fig. 1. Red line at median. Source numerical data are available in Source data.

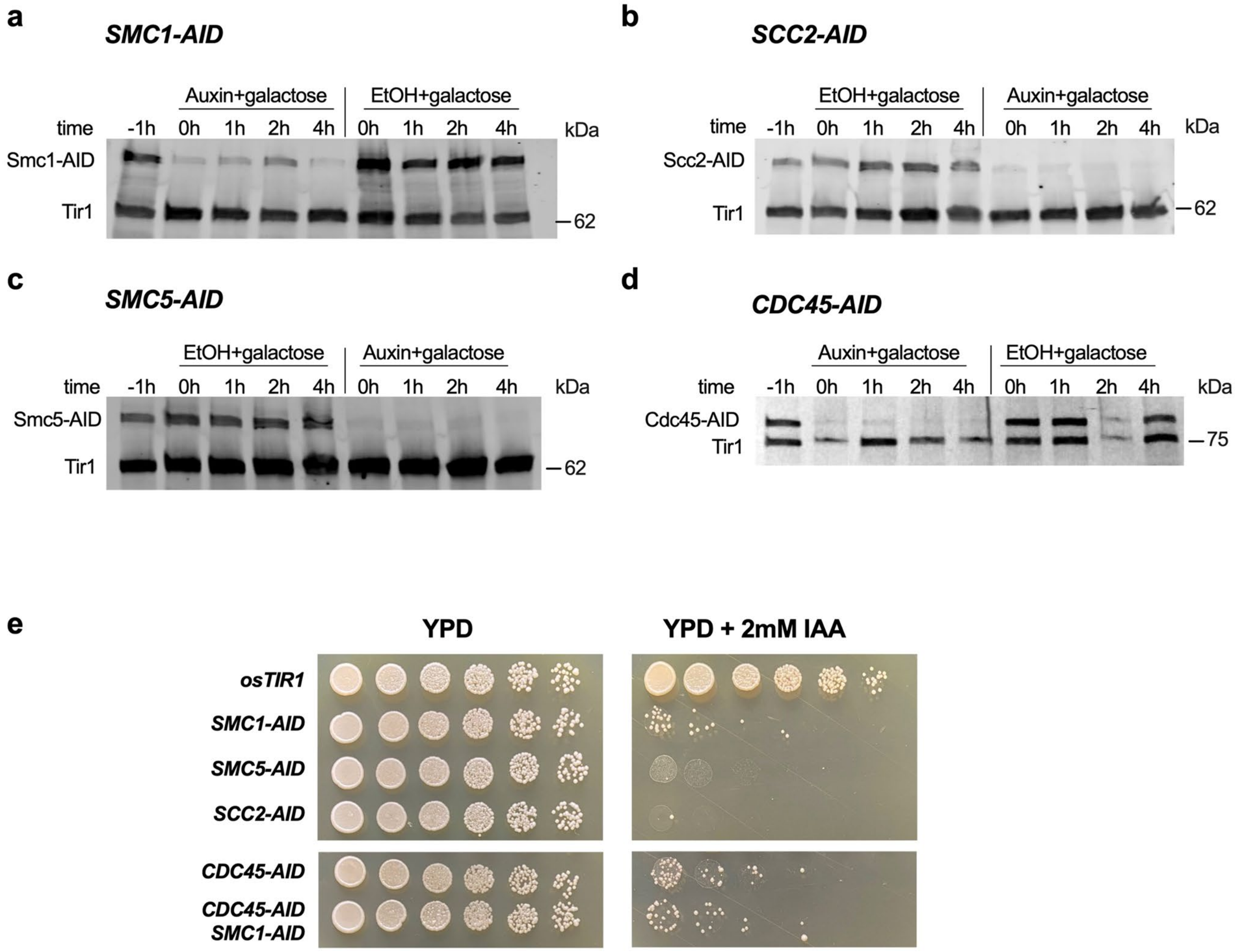

Extended Data Fig. 2 | Auxin induced degradation of target proteins leads to efficient depletion. **a**–**d**, anti-myc Western blots showing protein levels of 9myc-AID tagged proteins treated with auxin or ethanol used throughout microscopy DSB end-tethering assays. t-1h (before IAA/EtOH addition), t0h (1 hour IAA/EtOH), t1h (2 hours IAA/EtOH including 1 hour with galactose), t2h (3 hours IAA/EtOH including 2 hours with galactose) and t4h (5 hours IAA/EtOH including 4 hours with galactose). n = 3 biological replicates **e**, Drop assay of tethering strains on YPD and YPD + auxin, incubated for 48 hours at 30 °C. n = 2 biological replicates. Unprocessed blots are available in source data.

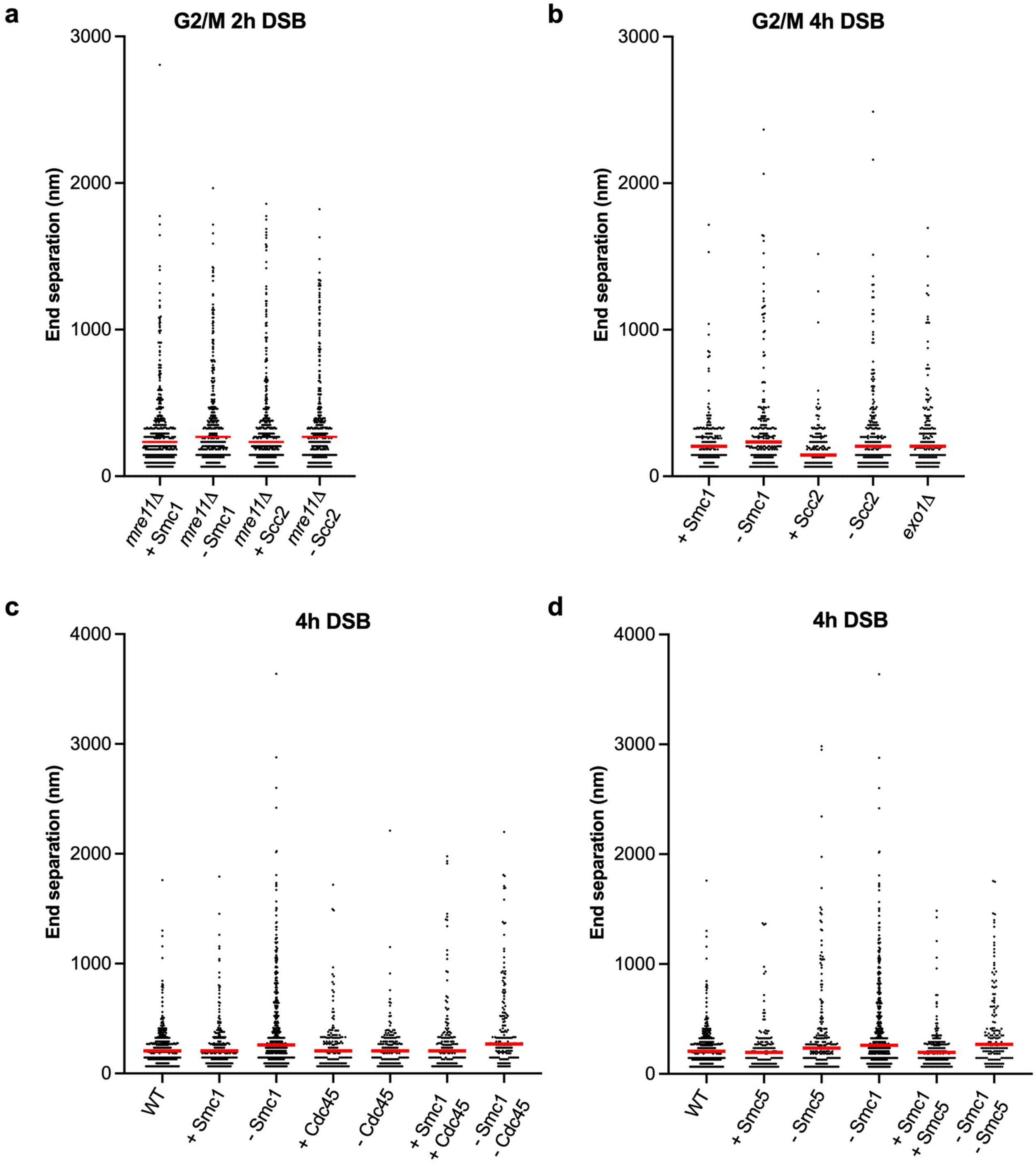

Extended Data Fig. 3 | Tethering data dot plots of Fig. 2. a–d, Scatter dot plots of end separation corresponding to the pool of measurements of biological replicates presented in Fig. 2. Red line at median. Source numerical data are available in Source data.

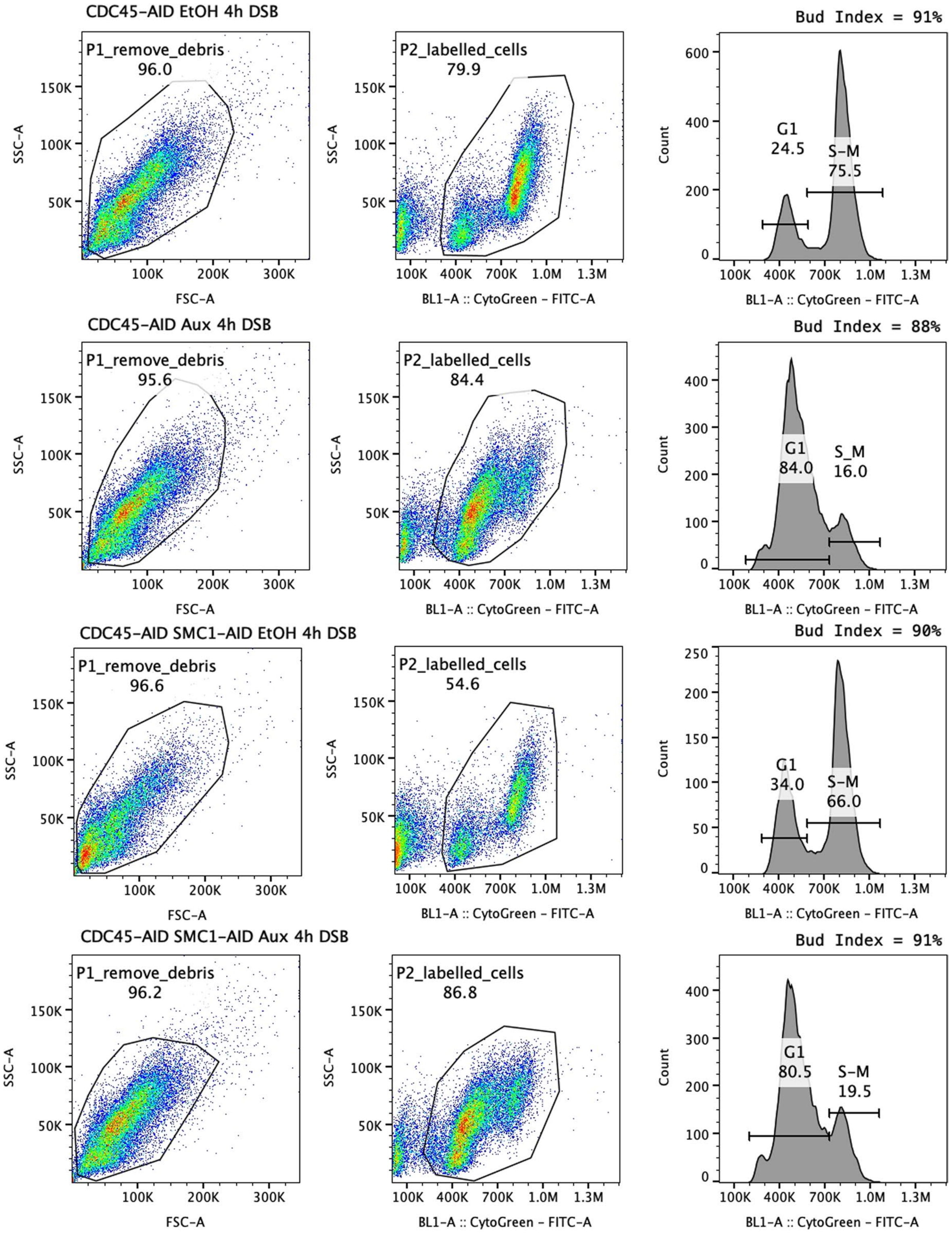

Extended Data Fig. 4 | Cdc45 degradation prevents genome duplication whilst allowing cells to proceed to G2/M. Gating strategy and fluorescent intensity profiles, determined by flow cytometry, showing cell cycle profiles of CDC45-AID and CDC45-AID SMC1-AID strains treated with IAA or EtOH after 4 h DSB induction. For each analysis the FSC/SCC (left panel) was gated to remove cellular debris and the uncolored cells were also removed by gating the FITC/SSC dot plot (middle panel). The FITC-A histogram was then plotted to get the cell cycle profile (right panel). The percentage of cells with 1n (G1) and 2n (S G2) DNA content is indicated for each strain. Percentage of cells with large buds is indicated above intensity profiles as bud index. n = 3 biological replicates.

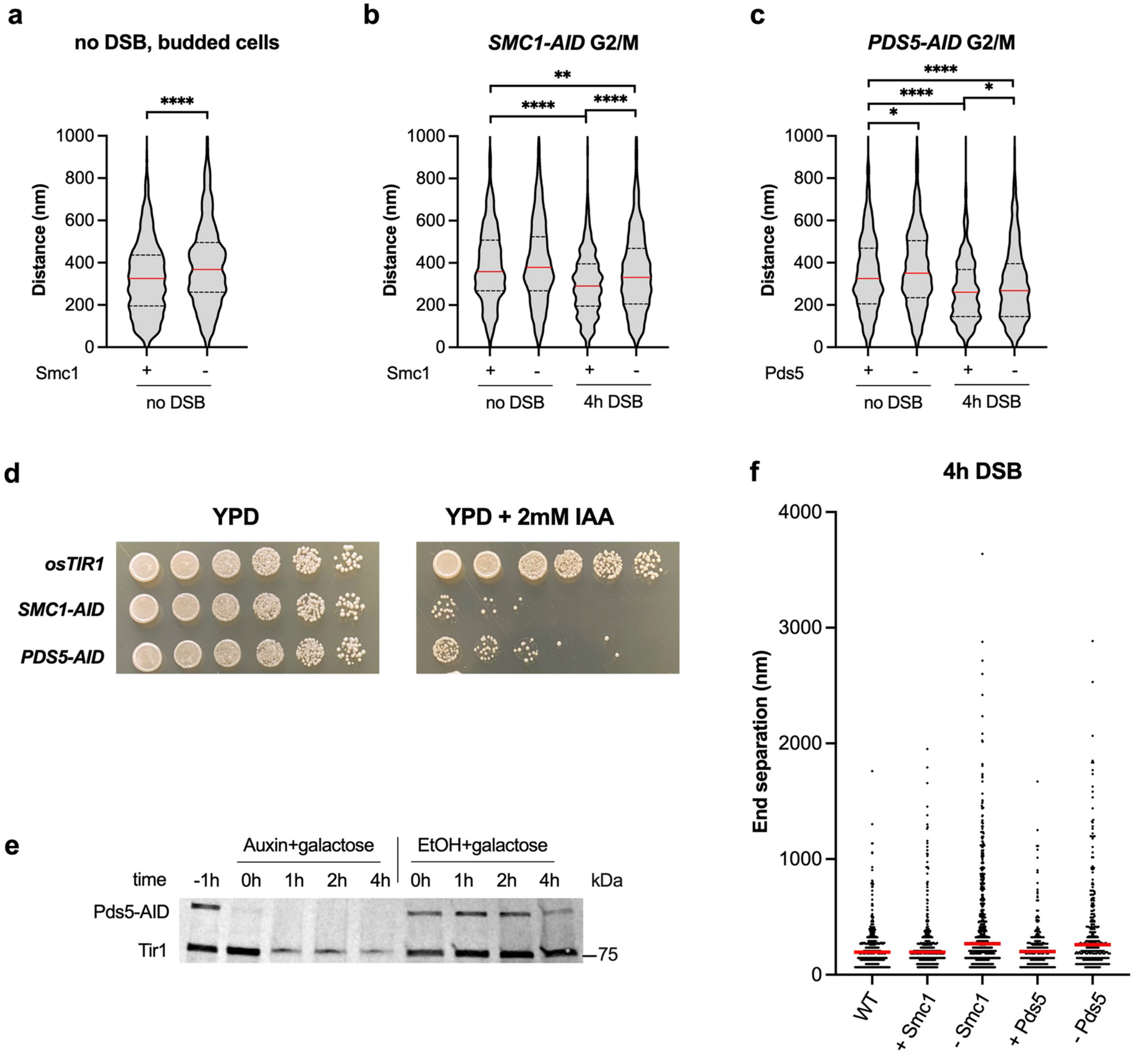

Extended Data Fig. 5 | Smc1 depletion reveals cohesin-dependent Pds5-independent genome compaction in S-M phase cells. a, Distances between 45 kb separated tags from the three biological replicas for SMC1-AID tagged strain treated with ethanol (+Smc1) or auxin (-Smc1) in Fig. 3c, represented as a violin plot. Red line at median, quartiles represented by dashed line. **b**, **c**, Distances between 45 kb separated tags from three biological replicas for SMC1-AID and PDS5-AID tagged strains arrested with nocodazole, treated with ethanol or auxin and following 4 hours DSB in Fig. 3d,e, represented as a violin plot. Red line at median, quartiles represented by dashed line. **d**, Drop assay of compaction strains plated on YPD and YPD + auxin, incubated for 48 hours at 30 °C. n = 2 biological replicates. **e**, anti-myc Western blot demonstrating protein levels of PDS5-AID strains treated with auxin or ethanol used throughout microscopy DSB end-tethering assay time course. t-1h (before IAA/EtOH addition), t0h (1 hour IAA/EtOH), t1h (2 hours IAA/EtOH including 1 hour with galactose), t2h (3 hours IAA/EtOH including 2 hours with galactose) and t4h (5 hours IAA/EtOH including 4 hours with galactose). n = 2 biological replicates **f**, Scatter dot plots of end separation corresponding to the pool of measurements of biological replicates presented in Fig. 3f. Red line at median. P values were calculated using a two-tailed unpaired Mann Whitney test. (*$P \leq 0.05$, **$P \leq 0.01$, ***$P \leq 0.001$, ****$P \leq 0.0001$, not significant (ns) $P > 0.05$). Numerical P values are indicated in Supplementary Information Table 4. (**a**) no DSB +Smc1 vs no DSB -Smc1 $P < 0.0001$. (**b**) no DSB +Smc1 vs 4 h DSB +Smc1 $P < 0.0001$, 4 h DSB +Smc1 vs 4 h DSB -Smc1 $P < 0.0001$, no DSB +Smc1 vs 4 h DSB -Smc1 $P = 0.0032$. (**c**) no DSB +Pds5 vs no DSB -Pds5 $P = 0.0169$, no DSB +Pds5 vs 4 h DSB +Pds5 $P < 0.0001$, no DSB +Pds5 vs 4 h DSB -Pds5 $P < 0.0001$, 4 h DSB +Pds5 vs 4 h DSB -Pds5 $P = 0.0101$. Source numerical data and unprocessed blots are available in Source data.

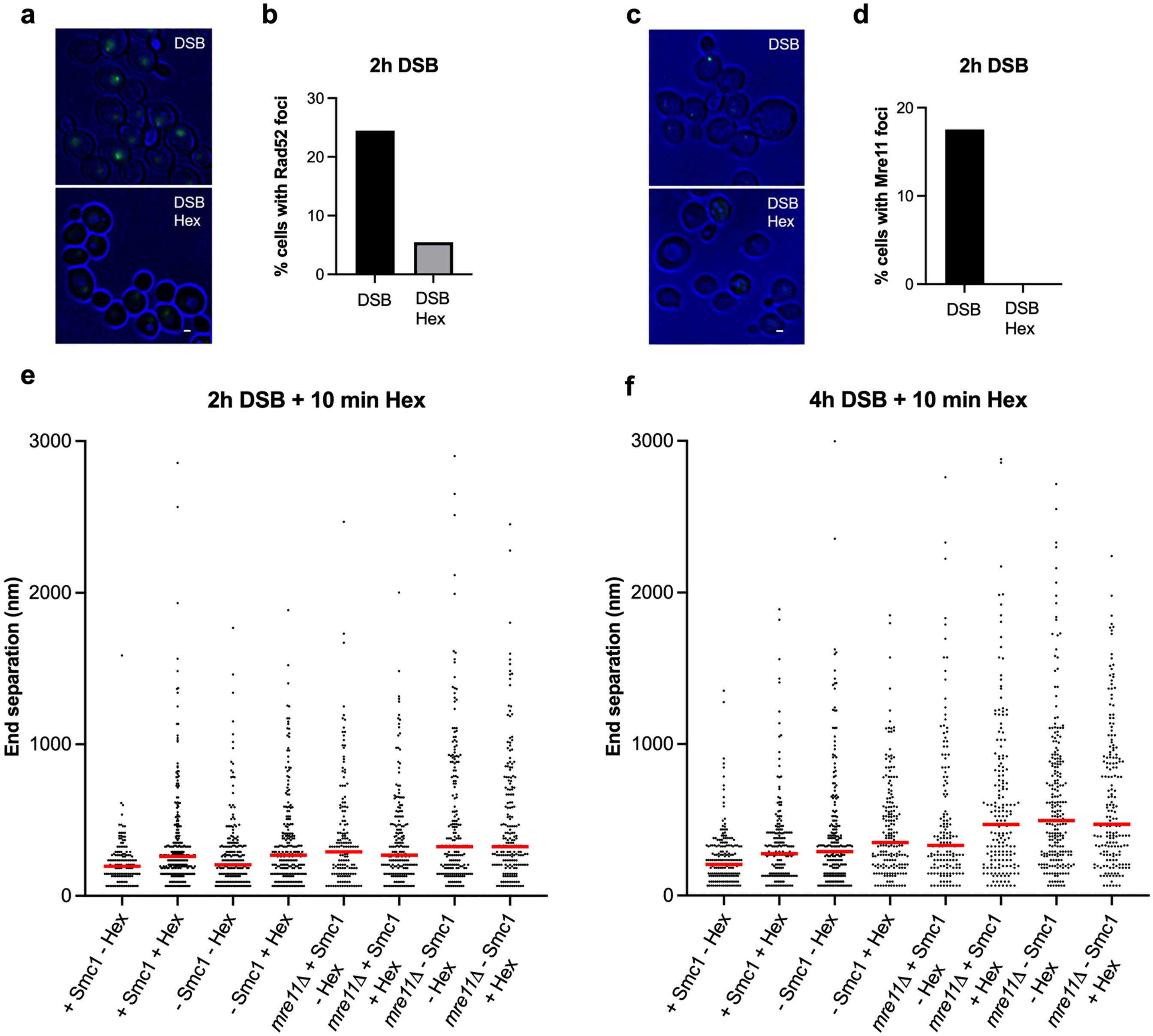

Extended Data Fig. 6 | Hexanediol abolishes Rad52 and Mre11-GFP foci and cohesin-dependent tethering in absence of MRX. **a**–**c**, Representative images of Rad52-YFP (**a**) and Mre11-GFP (**c**) foci at 2 h DSB with no treatment (DSB), or 30 minutes digitonin + hexanediol (DSB Hex) treatment. The images are maximum intensity projections and are representative of cells quantified in **b**–**d**. Scale bars, 1 µm. **b**–**d**, Quantification of cells with Rad52-YFP (**b**) and Mre11-GFP (**d**) foci at 2 h DSB with no treatment (DSB), or 30 minutes digitonin + hexanediol (DSB Hex) treatment. Data represent the analysis of N = 188 (b, DSB), N = 146 (b, DSB Hex), N = 97 (d, DSB) and 126 (d, DSB Hex) cells. **e**, **f**, Scatter dot plots of end separation corresponding to the pool of measurements of biological replicates presented in Fig. 4c,d. Red line at median. Source numerical data are available in Source data.

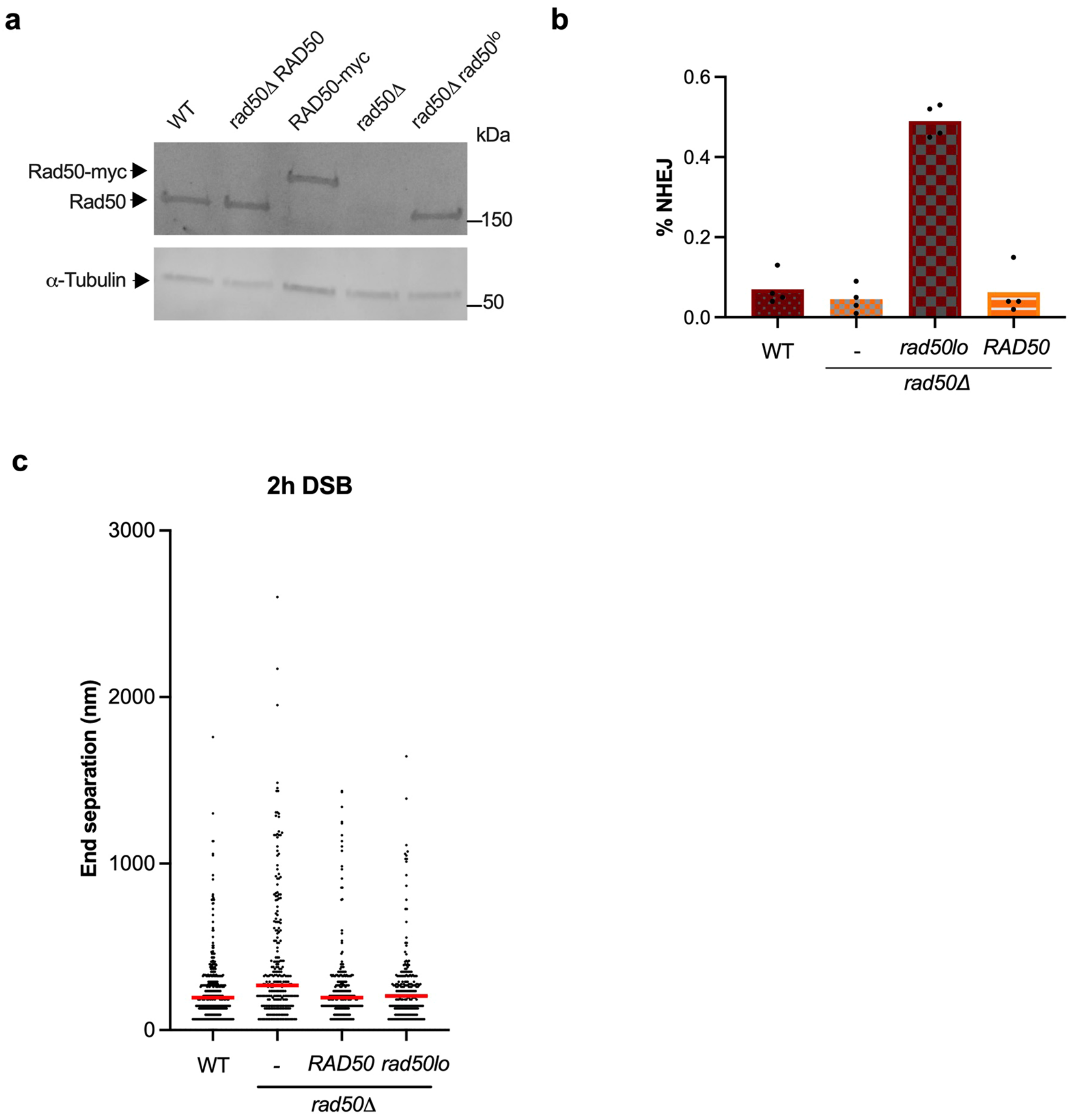

Extended Data Fig. 7 | The rad50lo mutant protein is expressed and proficient for NHEJ. a, anti-Rad50 western blot showing protein levels in the indicated strains with tubulin as a loading control. n = 2 biological replicate. **b**, Percentage of cell survival on galactose plate demonstrating NHEJ efficiency in the indicated strains. n = 4 biological replicates **c**, Scatter dot plots of end separation corresponding to the pool of measurements of biological replicates presented in Fig. 5a. Red line at median. Source numerical data and unprocessed blots are available in Source data.

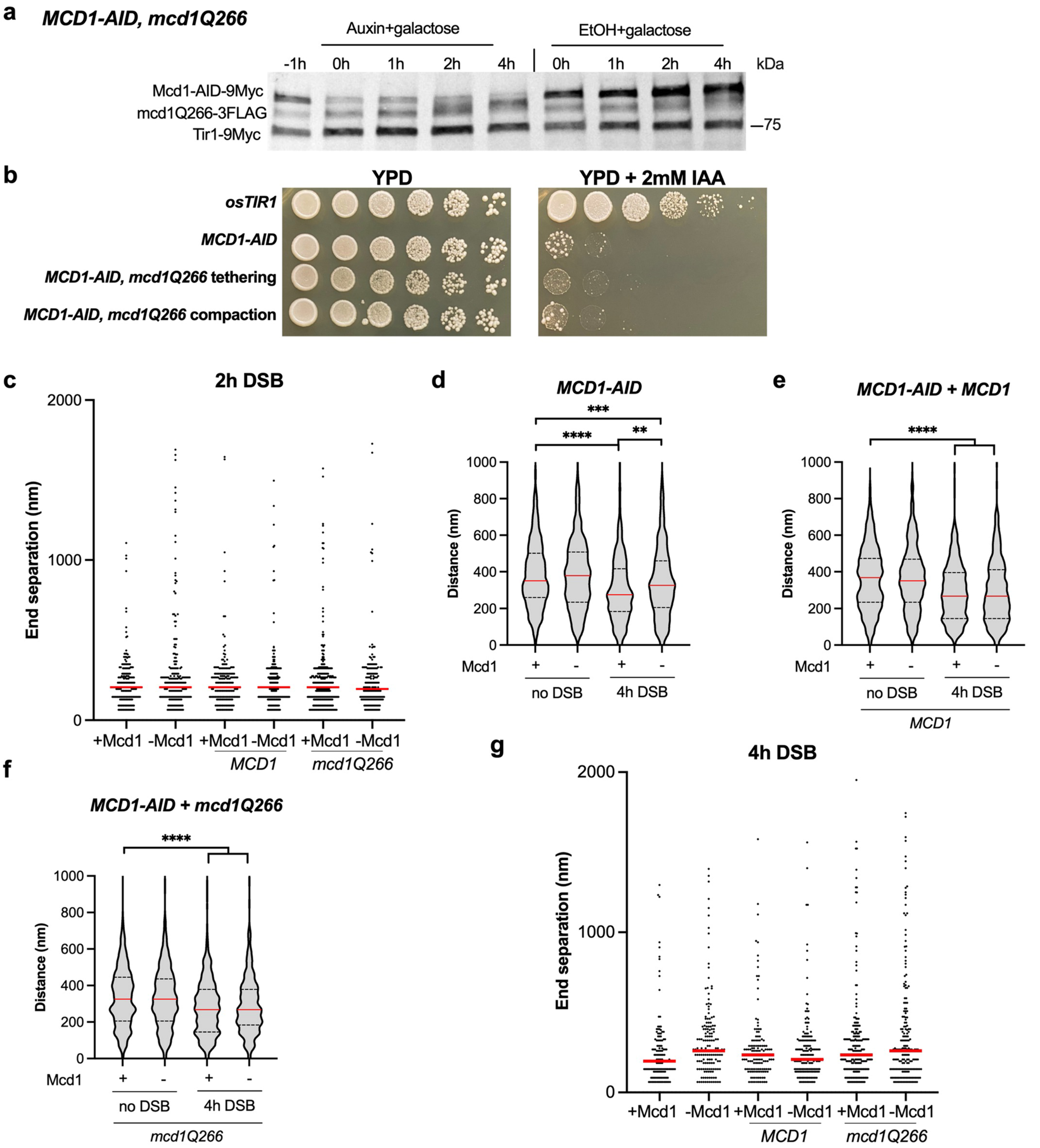

Extended Data Fig. 8 | See next page for caption.

Extended Data Fig. 8 | mcd1Q266 rescues DSB dependent genome compaction in the absence of Mcd1. a, anti-myc/anti-flag Western blots demonstrating protein levels of AID-myc and mcd1Q266-FLAG tagged proteins treated with auxin or ethanol throughout microscopy DSB end-tethering assays. t-1h (before IAA/EtOH addition), t0h (1 hour IAA/EtOH), t1h (2 hours IAA/EtOH including 1 hour with galactose), t2h (3 hours IAA/EtOH including 2 hours with galactose) and t4h (5 hours IAA/EtOH including 4 hours with galactose). n = 3 biological replicates. **b**, Drop assay of MCD1 strains on YPD and YPD + auxin, incubated for 72 hours at 23 °C. n = 2 biological replicates. **c**, Scatter dot plots of end separation corresponding to the pool of measurements of biological replicates presented in Fig. 5c. Red line at median. **d**–**f**, Distances between 45 kb separated tags from three individual replicas for *MCD1-AID* tagged strains complemented with nothing, *MCD1*, or *mcd1Q266*, treated with ethanol or auxin and nocodazole after 4 h DSB, represented as a violin plot. Red line at median, quartiles represented by dashed line. **g**, Scatter dot plots of end separation corresponding to the pool of measurements of biological replicates presented in Fig. 5f. Red line at median. *P* values were calculated using a two-tailed unpaired Mann Whitney test. (*$P \leq 0.05$, **$P \leq 0.01$, ***$P \leq 0.001$, ****$P \leq 0.0001$, not significant (ns) $P > 0.05$). Numerical *P* values are indicated in Supplementary Information Table 4. (**d**) no DSB +Mcd1 vs 4 h DSB +Mcd1 $P < 0.0001$, no DSB +Mcd1 vs 4 h DSB -Mcd1 $P = 0.0004$, 4 h DSB +Mcd1 vs 4 h DSB -Mcd1 $P = 0.0012$. (**e**) no DSB *MCD1* +Mcd1 vs 4 h DSB *MCD1* +Mcd1 $P < 0.0001$, no DSB *MCD1* +Mcd1 vs 4 h DSB *MCD1* -Mcd1 $P < 0.0001$. (**f**) no DSB *mcd1Q266* +Mcd1 vs 4 h DSB *mcd1Q266* +Mcd1 $P < 0.0001$, no DSB *MCD1* +Mcd1 vs 4 h DSB *MCD1* -Mcd1 $P < 0.0001$. Source numerical data and unprocessed blots are available in Source data.

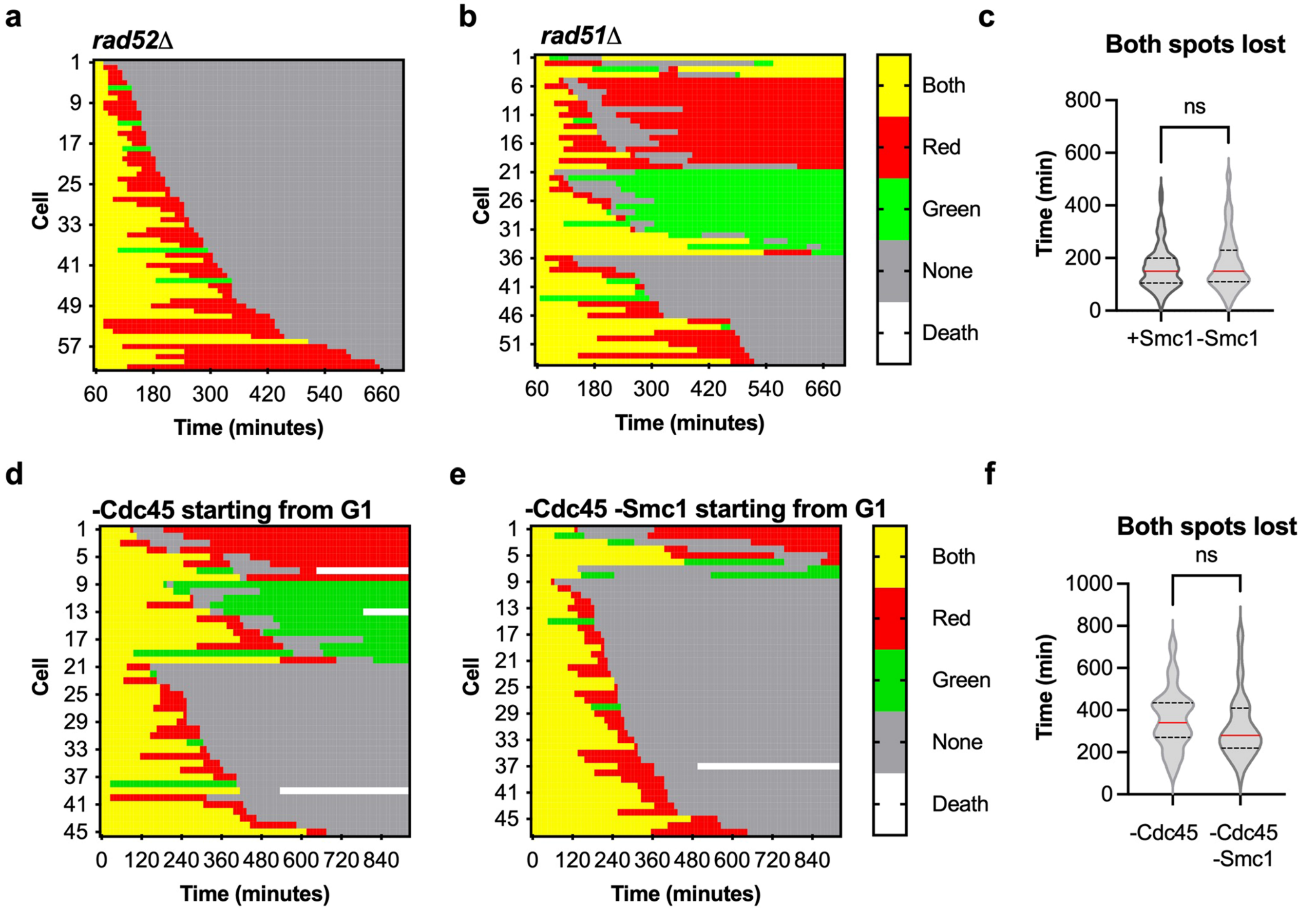

Extended Data Fig. 9 | Cohesin depletion does not alter rate of resection following DSB. a, **b**, Spot characteristics of individual cells in *rad52Δ* and *rad51Δ* cells during a 12 hour period after DNA DSB induction. Yellow represents presence of red and green spots, red represents presence of red spot only, green represents presence of green spot only, grey represents the presence of no spots, and white represents cell death. Images were acquired every ten minutes at each position on a microfluidic plate. Data represent N = 61 (*rad52Δ*), N = 54 (*rad51Δ*) cells from n = 2 independent experiments **c**, Time taken for loss of both red and green spots after DSB induction in microfluidic experiments for *SMC1-AID* strains shown in Fig. 6e,f. Red line at median, quartiles represented by dashed line. Data represent N = 77 (+Smc1) and N = 79 (-Smc1) cells from n = 2 independent experiments. **d**, **e**, Spot characteristics of individual cells in *CDC45-AID*, *CDC45-AID SMC1-AID* cells during a 15.5 hour period after DNA DSB induction. DSB was induced in the microfluidic plate, and images were acquired every ten minutes at each position on a microfluidic plate. Data represent N = 45 (-Cdc45) and N = 47 (-Cdc45 -Smc1) cells from n = 3 (-Cdc45) and n = 2 (-Cdc45 -Smc1) independent experiments. **f**, Time taken for loss of both red and green spots after DSB induction in microfluidic experiments for auxin exposed *CDC45-AID* and *CDC45-AID SMC1-AID* strains shown in panels d-e. Red line at median, quartiles represented by dashed line. P values were calculated using a two-tailed unpaired Mann Whitney test. (**P* ≤ 0.05, ***P* ≤ 0.01, ****P* ≤ 0.001, *****P* ≤ 0.0001, not significant (ns) *P* > 0.05). Numerical *P* values are indicated in Supplementary Information Table 4. (**c**) + Smc1 vs -Smc1 *P* = 0.5292. (**d**) -Cdc45 vs -Cdc45 -Smc1 *P* = 0.0731. Source numerical data are available in Source data.

nature portfolio

Corresponding author(s): Dubrana Karine

Last updated by author(s): Sep 4, 2024

Reporting Summary

Nature Portfolio wishes to improve the reproducibility of the work that we publish. This form provides structure for consistency and transparency in reporting. For further information on Nature Portfolio policies, see our Editorial Policies and the Editorial Policy Checklist.

Statistics

For all statistical analyses, confirm that the following items are present in the figure legend, table legend, main text, or Methods section.

n/a	Confirmed	
☐	☒	The exact sample size (*n*) for each experimental group/condition, given as a discrete number and unit of measurement
☐	☒	A statement on whether measurements were taken from distinct samples or whether the same sample was measured repeatedly
☐	☒	The statistical test(s) used AND whether they are one- or two-sided *Only common tests should be described solely by name; describe more complex techniques in the Methods section.*
☒	☐	A description of all covariates tested
☒	☐	A description of any assumptions or corrections, such as tests of normality and adjustment for multiple comparisons
☐	☒	A full description of the statistical parameters including central tendency (e.g. means) or other basic estimates (e.g. regression coefficient) AND variation (e.g. standard deviation) or associated estimates of uncertainty (e.g. confidence intervals)
☒	☐	For null hypothesis testing, the test statistic (e.g. *F*, *t*, *r*) with confidence intervals, effect sizes, degrees of freedom and *P* value noted *Give P values as exact values whenever suitable.*
☒	☐	For Bayesian analysis, information on the choice of priors and Markov chain Monte Carlo settings
☒	☐	For hierarchical and complex designs, identification of the appropriate level for tests and full reporting of outcomes
☒	☐	Estimates of effect sizes (e.g. Cohen's *d*, Pearson's *r*), indicating how they were calculated

Our web collection on statistics for biologists contains articles on many of the points above.

Software and code

Policy information about availability of computer code

Data collection	Image data collection: Metamorph (Molecular Device, v7.10.5) FACS data collection: Western Blot data collection: Image Studio Software v5 Real-time PCR data collection: StepOne Software (Applied Biosciences, v2.0)
Data analysis	FACS analysis: FlowJo (BD Biosciences, v10.10) Statistical analysis: PRISM (GraphPad, v10.3.1) Imaging data analysis: Fiji ImageJ (NIH, ImageJ2 v2.14.0/1.54f) Real-time qPCR analysis: Microsoft Excel for Mac (v16.88)

For manuscripts utilizing custom algorithms or software that are central to the research but not yet described in published literature, software must be made available to editors and reviewers. We strongly encourage code deposition in a community repository (e.g. GitHub). See the Nature Portfolio guidelines for submitting code & software for further information.

Data

Policy information about availability of data

All manuscripts must include a data availability statement. This statement should provide the following information, where applicable:

- Accession codes, unique identifiers, or web links for publicly available datasets
- A description of any restrictions on data availability
- For clinical datasets or third party data, please ensure that the statement adheres to our policy

Source data are provided with this paper. All data supporting the findings in this study are available in the main text or the supplementary material (numerical source data and unprocessed blot images). Strains and raw images quantified but not shown in the paper are available upon request.

Research involving human participants, their data, or biological material

Policy information about studies with human participants or human data. See also policy information about sex, gender (identity/presentation), and sexual orientation and race, ethnicity and racism.

Reporting on sex and gender	N/A
Reporting on race, ethnicity, or other socially relevant groupings	N/A
Population characteristics	N/A
Recruitment	N/A
Ethics oversight	N/A

Note that full information on the approval of the study protocol must also be provided in the manuscript.

Field-specific reporting

Please select the one below that is the best fit for your research. If you are not sure, read the appropriate sections before making your selection.

☒ Life sciences ☐ Behavioural & social sciences ☐ Ecological, evolutionary & environmental sciences

For a reference copy of the document with all sections, see nature.com/documents/nr-reporting-summary-flat.pdf

Life sciences study design

All studies must disclose on these points even when the disclosure is negative.

Sample size	no statistical method was used to pre-determine sample size. The number of independent experiments is a standard sample size to accurately detect differences in cell biology experiments.
Data exclusions	The imaging data were excluded from analysis when poor signal did not allow analysis
Replication	Reproducibility was verified using biological replicates and independent experiments. In addition, analysis of a large amount (50 to 100) of single cells per experiment was used to assess reproducibility of microfluidics experiments . All the experiments have been succesfully replicated using appropriate negative controls in each replicate.
Randomization	Randomization was not relevant in the experiments presented in this study as yeast cultures are uniform on a population level. For most single-cell microscopy experiments all cells with a signal were were included in the analysis from an overview of asynchronous populations. However, for single-cell microscopy experiments involving Cdc45 depleted cells, only cells in G1 at the beginning of the experiments were analyzed.
Blinding	Data were analyzed using semi-automated methods. In case where manual filtering was incorporated, same criteria were applied to all strains or treatment under investigation. The Investigators were not blinded to allocation during experiments and outcome assessment as each experiment was performed by an individual investigator who was aware of the experimental groups and treatments. However, some experiments were replicated by different investigators.

Reporting for specific materials, systems and methods

We require information from authors about some types of materials, experimental systems and methods used in many studies. Here, indicate whether each material, system or method listed is relevant to your study. If you are not sure if a list item applies to your research, read the appropriate section before selecting a response.

Materials & experimental systems

n/a	Involved in the study
☐	☒ Antibodies
☒	☐ Eukaryotic cell lines
☒	☐ Palaeontology and archaeology
☒	☐ Animals and other organisms
☒	☐ Clinical data
☒	☐ Dual use research of concern
☒	☐ Plants

Methods

n/a	Involved in the study
☒	☐ ChIP-seq
☐	☒ Flow cytometry
☒	☐ MRI-based neuroimaging

Antibodies

Antibodies used	Primary antibodies: - Anti-MYC (WB 1:1000; Anti-Myc tag antibody [9E10] Abcam ab32) - Anti-FLAG (WB 1:4000; ANTI-FLAG® M2 antibody Sigma-Aldrich F3165) - Anti-Rad50 (WB 1:1000; PA5-32176 invitrogen) Secondary antibodies: - Goat anti-Rabbit IgG (H+L) Highly Cross-Adsorbed Secondary Antibody Alexa Fluor™ Plus 800 (WB 1:10000; Invitrogen A32735) - Goat anti-Mouse IgG (H+L) Highly Cross-Adsorbed Secondary Antibody, Alexa Fluor™ Plus 680 (WB 1:10000; Invitrogen A32729) - Goat anti-Mouse IgG (H+L) Highly Cross-Adsorbed Secondary Antibody, Alexa Fluor™ Plus 800 (WB 1:10000; Invitrogen A32730)
Validation	Validation for primary antibodies was provided by the supplier or selected publications as indicated: 1- Anti-MYC validated by manufacturer Abcam (Manufacturers information available at https://doc.abcam.com/datasheets/active/ab32/en-us/myc-tag-antibody-9e10-ab32.pdf) 2- Anti-FLAG validated by manufacturer Millipore Sigma(Manufacturers information available at https://www.sigmaaldrich.com/specification-sheets/120/274/F3165-BULK.pdf) 3- anti-Rad50 (Marsella A, Gobbini E, Cassani C, Tisi R, Cannavo E, Reginato G, Cejka P, Longhese MP. Sae2 and Rif2 regulate MRX endonuclease activity at DNA double-strand breaks in opposite manners. Cell Rep. 2021 Mar 30;34(13):108906. doi: 10.1016/j.celrep.2021.108906.) 3- anti-Rad50 Kissling VM, Reginato G, Bianco E, Kasaciunaite K, Tilma J, Cereghetti G, Schindler N, Lee SS, Guérois R, Luke B, Seidel R, Cejka P, Peter M. Mre11-Rad50 oligomerization promotes DNA double-strand break repair. Nat Commun. 2022 May 2;13(1):2374. doi: 10.1038/s41467-022-29841-0)

Plants

Seed stocks	N/A
Novel plant genotypes	N/A
Authentication	N/A

Flow Cytometry

Plots

Confirm that:

☒ The axis labels state the marker and fluorochrome used (e.g. CD4-FITC).

☒ The axis scales are clearly visible. Include numbers along axes only for bottom left plot of group (a 'group' is an analysis of identical markers).

☒ All plots are contour plots with outliers or pseudocolor plots.

☒ A numerical value for number of cells or percentage (with statistics) is provided.

Methodology

Sample preparation	0.5 OD600nm of cells were fixed in ethanol 70% and stored at -20°C. Cells were pelleted, washed, and then incubated in Sodium Citrate pH7.4 50mM with 0.25mg/ml RNAseA for 1 hour at 50°C. Proteinase K was then added, to a final

	concentration of 2mg/ml, and incubated for further 1 hour at 50°C. Cells were pelleted, and then stained in a pH7.4 50mM Sodium Citrate solution containing 1µM SYTOX Green Nucleic Acid Stain (Invitrogen – S7020). Cells were sonicated.
Instrument	Novocyte cytometer (ACEA bioscience.Inc)
Software	FlowJo software (BD Biosciences, v10.10)
Cell population abundance	N/A
Gating strategy	the FSC/SCC was gated to remove cellular debris and the uncolored cells were also removed by gating the FITC/SSC dot plot . The FITC-A histogram was then plotted to get the cell cycle profile.

☒ Tick this box to confirm that a figure exemplifying the gating strategy is provided in the Supplementary Information.